The prolactin receptor scaffolds Janus kinase 2 via co-structure formation with phosphoinositide-4,5-bisphosphate

Raul Araya-Secchi[1,2], Katrine Bugge[3#], Pernille Seiffert[3#], Amalie Petry[4], Gitte W. Haxholm[3], Kresten Lindorff-Larsen[3], Stine F. Pedersen[4*], Lise Arleth[1*] and Birthe B. Kragelund[3*],

[1]Structural Biophysics, Section for Neutron and X-ray Science, Niels Bohr Institute, University of Copenhagen, 2100 Copenhagen, Denmark.
[2]Facultad de Ingenieria Arquitectura y Diseño, Universidad San Sebastian, Bellavista 7, Santiago, Chile.
[3]Structural Biology and NMR Laboratory (SBiNLab), Department of Biology, University of Copenhagen, 2200 Copenhagen, Denmark.
[4]Section for Cell Biology and Physiology, Department of Biology, University of Copenhagen, 2200 Copenhagen N, Denmark

#contributed equally

*Corresponding author: bbk@bio.ku.dk.
Correspondence also to arleth@nbi.ku.dk and sfpedersen@bio.ku.dk

Running title: Co-structure formation by PRLR, JAK2 and PI(4,5)P_2

Abstract

Class 1 cytokine receptors transmit signals through the membrane by a single transmembrane helix to an intrinsically disordered cytoplasmic domain that lacks kinase activity. While specific binding to phosphoinositides has been reported for the prolactin receptor (PRLR), the role of lipids in PRLR signalling is unclear. Using an integrative approach combining NMR spectroscopy, cellular signalling experiments, computational modelling and simulation, we demonstrate co-structure formation of the disordered intracellular domain of the human PRLR, the membrane constituent phosphoinositide-4,5-bisphosphate (PI(4,5)P_2) and the FERM-SH2 domain of the Janus kinase 2 (JAK2). We find that the complex leads to accumulation of PI(4,5)P_2 at the transmembrane helix interface and that mutation of residues identified to interact specifically with PI(4,5)P_2 negatively affects PRLR-mediated activation of signal transducer and activator of transcription 5 (STAT5). Facilitated by co-structure formation, the membrane-proximal disordered region arranges into an extended structure. We suggest that the co-structure formed between PRLR, JAK2 and PI(4,5)P_2 locks the juxtamembrane disordered domain of the PRLR in an extended structure, enabling signal relay from the extracellular to the intracellular domain upon ligand binding. We find that the co-structure exists in different states which we speculate could be relevant for turning signalling on and off. Similar co-structures may be relevant for other non-receptor tyrosine kinases and their receptors.

Keywords: IDP, NMR, simulation, prolactin receptor, JAK2, single-pass transmembrane receptors, PI(4,5)P_2,

Introduction

Cytokine receptors are transmembrane glycoproteins that bind cytokines on the cell surface and transduce signals across the membrane to the interior of the cell. This, in turn, activates signalling pathways leading to multiple outcomes including induction of immune responses, cell proliferation, altered metabolism and differentiation (Brooks et al., 2016). Class 1 cytokine receptors constitute a subclass of receptors that transverse the membrane by a single α-helical transmembrane domain (TMD) (Brooks et al., 2016), separating a folded extracellular domain (ECD) from a disordered intracellular domain (ICD). The prolactin (PRL) receptor (PRLR) is one of the structurally most simple cytokine receptors (***Figure 1***). Signaling by the PRLR/PRL complex is implicated in the regulation of more than 300 biological functions in vertebrates (Bole-Feysot et al., 1998), and its function is especially well-known for its essential role in mammary gland development and lactation (Hannan et al., 2022). Apart from this, deregulation of PRLR/PRL signalling is associated with several pathologies in humans of which hyperprolactinemia resulting in reproductive failure is best described (Bachelot and Binart, 2007; Newey et al., 2013). Deregulation of PRLR/PRL signaling is linked to other diseases and, although still debated, suggested to be implicated in the development and progression of prostate (Sackmann-Sala and Goffin, 2015) and breast (Clevenger and Rui, 2022) cancers.

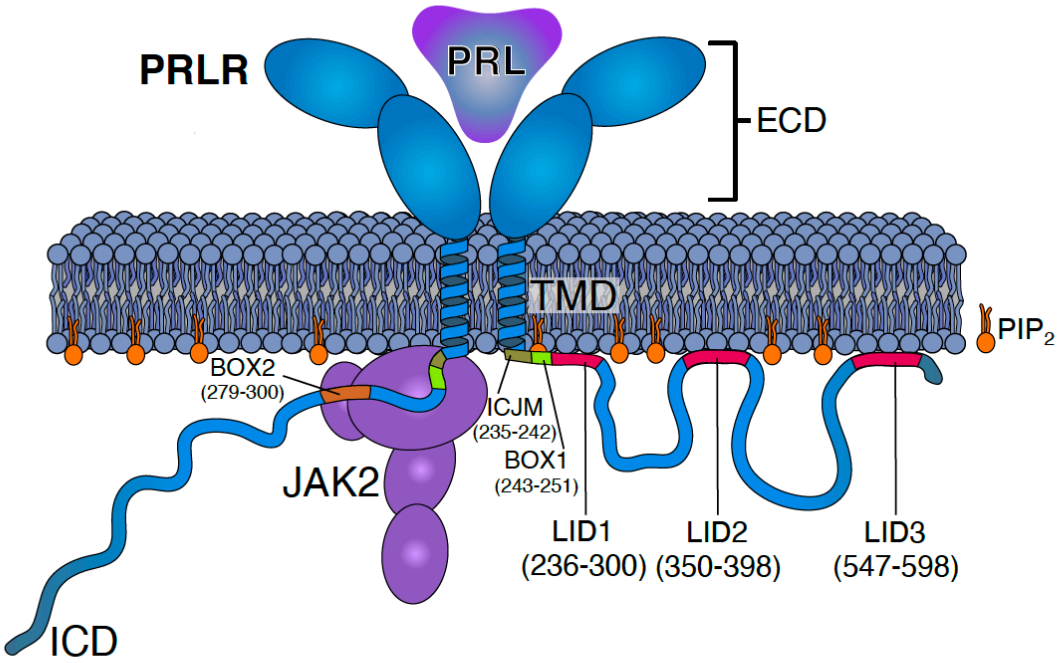

Fig. 1: Schematics of the PRLR:PRL:JAK2 complex in the membrane. The PRLR is shown in light blue, the PRL as a dark blue triangle, the PRLR-ICD as a disordered chain and JAK2 in purple. The PI(4,5)P_2 lipid (PIP_2) is shown in orange. The intracellular juxtamembrane (ICJM) region and BOX1 of PRLR-ICD are highlighted in green nuances, while the three LIDs as defined in Haxholm et al., (Haxholm et al., 2015) are highlighted in red. For simplicity only one of the two ICDs is shown associated with JAK2 via the BOX1 (green) and BOX2 (orange) motifs.

For cytokine receptors, signal transduction through the membrane is received by an ICD, which is intrinsically disordered and lacks kinase activity (Haxholm et al., 2015). Thus, association of

83 auxiliary kinases is mandatory for signalling, with the Janus kinases (JAK1–3) and the tyrosine kinase
84 TYK2 being the most thoroughly described (Brooks et al., 2016; Morris et al., 2018). A proline-rich
85 region constituting the so-called BOX1 motif close to the membrane, as well as a second hydrophobic
86 motif termed BOX2, are known to be essential for JAK binding (***Figure 1***) (Ferrao et al., 2018;
87 Rowlinson et al., 2008). However, although progress has been made in the molecular understanding
88 of cytokine binding and despite several structures of folded ECDs (Broutin et al., 2010; de Vos et al.,
89 1992), TMDs (Bocharov et al., 2018; Bugge et al., 2016), a complete receptor (Kassem et al., 2021)
90 and a receptor ICD in complex with JAK1 (Glassman et al., 2022) have emerged, it is still not clear
91 how the signal inside the cell is received by the disordered region to elicit and in turn control signal
92 transduction.
93
94 A subset of class 1 cytokine receptors form homodimers and trimeric complexes with their ligands,
95 with the main dimerization occurring in the TMDs (Brooks et al., 2014; Brown et al., 2005; Gadd
96 and Clevenger, 2006; Kubatzky et al., 2001; Seubert et al., 2003). This group includes the growth
97 hormone receptor (GHR), the erythropoietin receptor (EPOR), the thrombopoietin receptor (TPOR)
98 and the PRLR, which have become well-established paradigmatic models. Recently, signal
99 transduction by the GHR has been suggested to occur via a rotation of the transmembrane helices
100 within the dimer leading to a subsequent separation of the ICDs (Brooks et al., 2014; Brown et al.,
101 2005). A torque is hereby exerted on the associated JAK2s, which is thought to relieve inhibition by
102 the pseudokinase domains, initiating signalling. The ICDs of these receptors have been shown to be
103 highly disordered (Haxholm et al., 2015), a feature which is preserved in models of the PRLR (Bugge
104 et al., 2016) and the full-length GHR in nanodiscs (Kassem et al., 2021). This brings forward the
105 question of how signalling is orchestrated by disorder and how a disordered linker region between
106 the TMD and the region bound to the kinases can communicate and transduce information.
107
108 For both the PRLR and the GHR, lipid interaction domains (LID) with affinity for negatively charged
109 lipids have been identified in their ICDs (Haxholm et al., 2015). Common to both receptors is that
110 they contain a LID proximal to the membrane, directly overlapping with the JAK2 interaction sites,
111 BOX1 and BOX2 (Seiffert et al., 2020). Using nuclear magnetic resonance (NMR) spectroscopy we
112 identified three LIDs in the PRLR-ICD termed LID1, LID2 and LID3 (***Figure 1***) (Haxholm et al.,
113 2015) and using lipid dot-blots we showed that the PRLR-ICD has variable affinities for different
114 membrane constituents, including for different phosphoinositides (PIs). In particular, PRLR has a
115 distinct affinity for phosphoinositide-4,5-bisphosphate (PI(4,5)P_2) and lacks affinity for PI(3,4,5)P_2
116 (Haxholm et al., 2015). PIs are important constituents of the membrane and play key roles in
117 signalling, both as membrane interaction partners that can be specifically modulated by
118 phosphorylation (Carracedo and Pandolfi, 2008), and as secondary messengers (McLaughlin et al.,
119 2002; Suh and Hille, 2005). Indeed, some single-pass receptors contain conserved anionic lipid
120 interaction sites close to the membrane (Hedger et al., 2015a) and increasing evidence suggest lipid
121 interaction to take on important regulatory roles (McLaughlin et al., 2005; Metcalf et al., 2010).
122 Recently, the epidermal growth factor receptor (EGFR) was shown to sequester PI(4,5)P_2 by
123 accumulating it around the TMD regulating the dimer/monomer equilibrium and with a possible
124 positive feedback loop through the activation of the phospholipase C (PLC) – diacylglycerol (DAG)-

IP_3 pathways (Maeda et al., 2018). This will lead to subsequent conversion of $PI(4,5)P_2$ to $PI(3,4,5)P_3$ and hence depletion of $PI(4,5)P_2$ from the membrane. Similar depletion of $PI(4,5)P_2$ from the plasma membrane has been noted under hypoxia (Lu et al., 2022). For class 1 cytokine receptors the role of PIs in signalling is less clear.

In a cellular context, signalling-related proteins can be membrane anchored through modifications such as acylation (Patwardhan and Resh, 2010; Rawat et al., 2013; Rawat and Nagaraj, 2010) or via designated lipid-binding domains. This includes the four point-1, ezrin, radixin moesin (FERM) domain of radixin, focal adhesion kinase (FAK) and the protein tyrosine phosphatase L1 (PTPL1) (Bompard et al., 2003; Feng and Mertz, 2015; Hamada et al., 2000), the SH2 domains of the Src family kinases (Park et al., 2016; Sheng et al., 2016) and the FERM-SH2 domain of merlin (Mani et al., 2011). Thus, kinases and receptors can co-localize at the plasma membrane without necessarily being bound within a complex. It is, however, unclear whether such membrane co-localisation has functional consequences, such as enhancing signalling speed, and whether the membrane may act as an additional scaffolding platform that enhances binding via restriction in the two-dimensional plane.

Recent work on disorder in membrane proteins and on the interplay between membrane proteins and lipids have revealed the need for strong integrative methods, combining successfully various structural biology techniques, biophysics and computational biology (Basak et al., 2022; Larsen et al., 2022). These include NMR, small-angle X-ray scattering, crosslinking-mass spectrometry and single molecule fluorescence combined with molecular dynamics simulations (Chavent et al., 2018; Goretzki et al., 2023). These efforts have provided important insights into the role of lipids in regulation of membrane proteins. For TRPV4, a member of the TRP vanilloid channel family, it was shown that an autoinhibitory patch of the receptor competed with $PI(4,5)P_2$ binding at the membrane to attenuate channel activity, and MD simulation showed that lipid binding affected the ensemble dynamics(Goretzki et al., 2023). For EphA2, a receptor tyrosine kinase, an integrative study showed how PIs mediate the interaction between the kinase domains, facilitated by clustering of PIPs via binding to the receptor juxtamembrane domain (Chavent et al., 2018) further promoting conformation specific dimerization (Stefanski et al., 2021). Thus, studying dynamic processes at the membrane interface is an emerging field requiring integrative structural biology approaches for detailed atomic resolution information.

For the PRLR it is still not clear whether, and if so how, interactions between the ICD and the membrane impact signal transduction and association with JAK2. Nor is it understood how structural disorder can relay and transmit information from the TMD to initiate signalling. To shed light on the molecular details underlying a potential interplay between the receptor, membrane and kinase we focused on the human PRLR and its LID1 closest to the membrane, facilitating the first intracellular step in signaling. Using an integrative approach combining NMR spectroscopy, cell biology and computational modelling, we demonstrate the formation of a co-structure comprised of the disordered PRLR-ICD, the membrane constituent $PI(4,5)P_2$ and the FERM-SH2 domain of the JAK2. Facilitated by this co-structure, the disordered region closest to the membrane forms an extended structure, which

166 we suggest stabilizes the disordered domain, allowing signal relay from the extracellular to the
167 intracellular domain.
168
169 **Results**
170 **LID1 is disordered in solution and when tethered to the transmembrane helix**
171 Membrane interactions by PRLR-ICD have previously been studied in the absence of anchoring to
172 the TMD defining three LIDs, with LID1 closest to the membrane (Haxholm et al., 2015). Since
173 tethering would increase the local concentrations at the membrane and the ICD, this could affect
174 affinity, complex lifetime as well as the degree by which structure formation would be captured.
175 Furthermore, the first LID, LID1, is disordered and is located in the juxtamembrane region where it
176 is responsible for transmitting information on extracellular hormone binding to the bound JAK2. As
177 this constitutes the very first step on the intracellular side, and given the distance to the other two
178 LIDs (LID2 and LID3) and their disconnect from the TMD by long disordered regions, we focused
179 exclusively on LID1. We recombinantly expressed the TMD (residues 211–235 with numbering
180 corresponding to the processed protein) with five residues added at the two termini ($TMD_{F206\text{-}V240}$),
181 and the TMD with the first 35 residues of LID1, TMD-$ICD_{F206\text{-}S270}$ (***Figure 2A***). We then examined
182 their structural propensities in detergents and in small unilamellar vesicles (SUVs) by NMR
183 spectroscopy. In 1,2-dihexanoyl-sn-glycero-3-phosphocholine (DHPC) micelles, most of the TMD
184 resonances of the $TMD_{F206\text{-}V240}$ and TMD-$ICD_{F206\text{-}S270}$ variants were readily superimposable in the
185 ^{15}N,^{1}H-HSQC spectra (***Figure 2 - figure supplement 1***), suggesting that the conformation of the TMD
186 was not affected by the presence of the ICD. For the TMD-$ICD_{F206\text{-}S270}$, C^{α} NMR resonances were
187 collected for most of the disordered region, while backbone carbon resonances for the TMD, except
188 for A222, and the region G236-P246 immediately following it, were broadened beyond detection in
189 the 3D spectra, preventing assignments (***Figure 2B)***. This may suggest that the first ten residues of
190 the ICD interact with or are buried in the micelles, or are affected by the overall slower tumbling of
191 the micelle, whereas the complete overlap of the TMD residues in the ^{15}N-HSQC spectra confirm the
192 helical structure as seen previously. We assigned the backbone nuclei of the detectable resonances of
193 TMD-$ICD_{F206\text{-}S270}$ in DHPC micelles and compared the secondary chemical shifts (SCS) to those of
194 the ICD alone ($ICD_{G236\text{-}Q396}$) (***Figure 2C***). Whereas the region of the ICD that is undetected in TMD-
195 $ICD_{F206\text{-}S270}$ formed transient extended structures in the absence of the TMD, the observable parts
196 were highly similar suggesting lack of structure induction by TMD tethering or the micelles. In 1-
197 palmitoyl-2-oleoyl-sn-glycero-3-phosphocholine (POPC) SUVs, only the resonances of the most C-
198 terminal residues of TMD-$ICD_{F206\text{-}S270}$ were detectable; however, the chemical shifts suggested that
199 the residues were disordered (***Figure 2 – figure supplement 2***). Taken together, these results suggest
200 that most of the ICD residues remain disordered when tethered to the TMD and in the presence of a
201 neutral membrane mimetic.

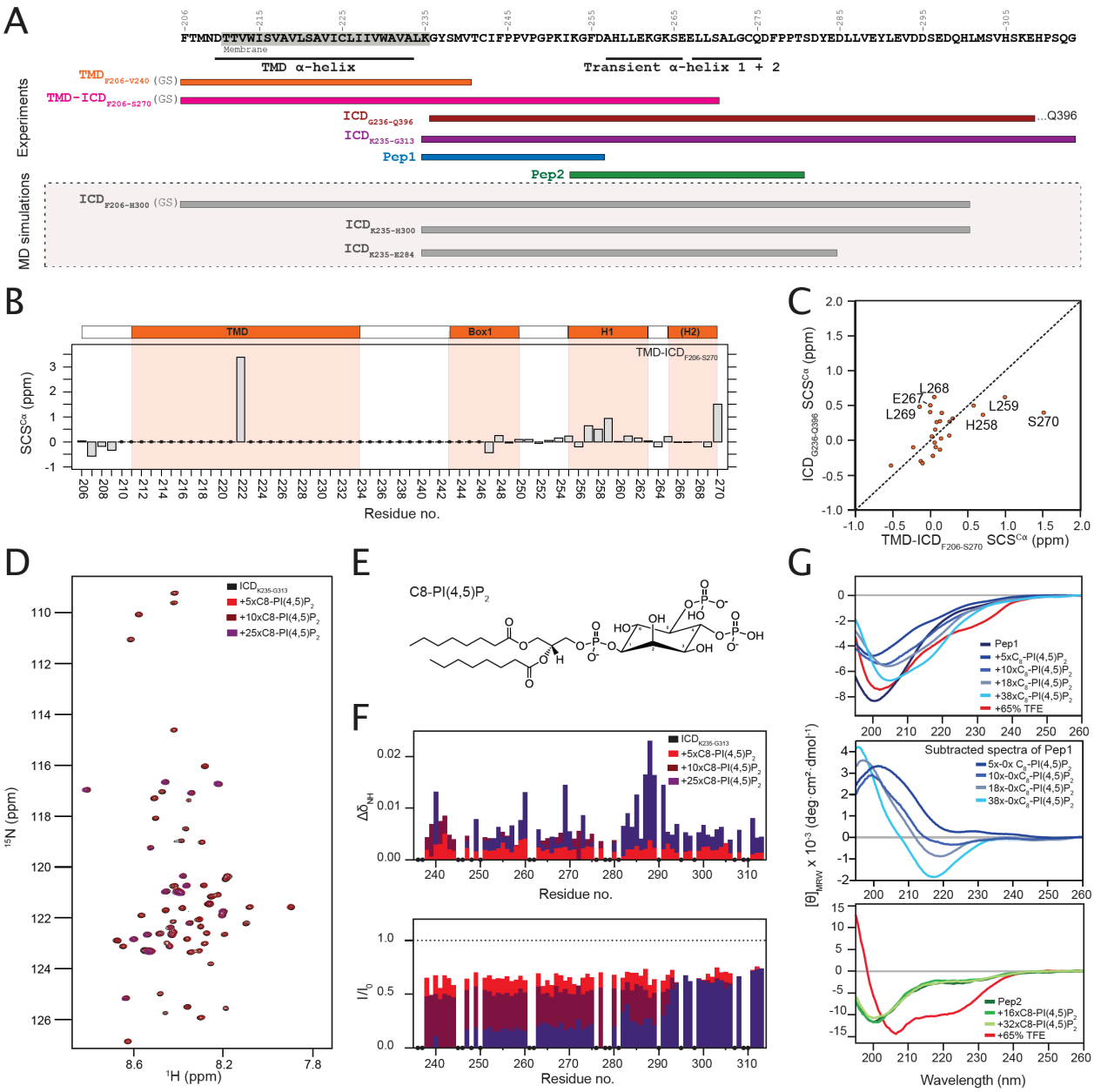

Fig. 2: The ICJM region of the PRLR interacts with PI(4,5)P$_2$. A) Overview of investigated PRLR variants. **B)** Secondary chemical shifts (SCSs) of TMD-ICD$_{F206-S270}$ reconstituted in DHPC micelles. **C)** Correlation plot of the SCSs of ICD$_{G236-Q396}$ plotted against those of TMD-ICD$_{F206-S270}$. **D)** ^{15}N,^{1}H-HSQC spectra of ^{15}N-ICD$_{K235-G313}$ titrated with 5x, 10x and 25x molar excess of C$_8$-PI(4,5)P$_2$. **E)** Structure of C$_8$-PI(4,5)P$_2$. **F)** Backbone amide chemical shift perturbations (CSPs) and peak intensity changes upon addition of C$_8$-PI(4,5)P$_2$ to ^{15}N-ICD$_{K235-G313}$ plotted against residue number. **G) Top**: Far-UV CD spectra of Pep1 titrated with C$_8$-PI(4,5)P$_2$ or in 65% TFE. **Middle:** Far-UV CD spectra of Pep1 in the presence of 5x-38x C$_8$-PI(4,5)P$_2$ subtracted with the spectrum of Pep1 in the absence of C$_8$-PI(4,5)P$_2$. **Bottom**: Far-UV CD spectra of Pep2 titrated with C$_8$-PI(4,5)P$_2$ or in 65% TFE**.** * indicate missing data points.

Figure supplement 1: *^{15}N, ^{1}H-HSQC spectra of A) TMD$_{F206-V240}$ and TMD-ICD$_{F206-S270}$ in DHPC micelles, and (B) TMD-ICD$_{F206-S270}$ in POPC SUVs.*

Figure supplement 2: *C$^{\alpha}$ secondary chemical shifts of ICD$_{G236-Q396}$*

217 **LID1 binds PI(4,5)P_2 in the juxtamembrane region forming extended structures**
218 PRLR-ICD has previously been shown to bind PI(4,5)P_2 (but not PI(3,4,5)P_3) (Haxholm et al., 2015),
219 suggesting that this lipid could modulate membrane affinity and the structural properties of the PRLR-
220 ICD. To separate headgroup effects from lipid bilayer surface effects, we used a short-chain C_8-
221 PI(4,5)P_2, which has a high critical micelle concentration (CMC) of 2 mM (Goñi et al., 2014) and
222 analysed the structural changes by NMR and CD spectroscopy at concentrations below the CMC
223 (Goñi et al., 2014) to identify the binding site.
224
225 ^{15}N-labelled $ICD_{K235-G313}$ covering LID1 (***Figure 1***) was titrated with C_8-PI(4,5)P_2 and binding was
226 assessed by ^{1}H-^{15}N-HSQC spectra (***Figure 2D-F***). The chemical shift perturbations (CSPs) were
227 modest whereas substantial intensity changes were observed throughout the chain, supporting a direct
228 interaction between the ICD and lipids. The resonances from G236-F244 completely disappeared
229 suggesting exchange on an intermediate NMR timescale, while intensities were substantially reduced
230 in the V247-S290 region (***Figure 2F***). In the region from D285-E292 we observed an almost inverse
231 correlation between the CSPs and the intensities. This suggests that in contrast to the preceding
232 region, a faster local exchange rate allows us to follow the resonances from the bound state in this
233 region, giving rise to the large CSPs. From this region and to the C-terminus, only moderate intensity
234 changes were observed (***Figure 2F***). These findings suggest that the primary PI(4,5)P_2 binding site
235 is located closest to the membrane in what we define as the intracellular juxtamembrane (ICJM)
236 region (K235-C242). The ICJM is located N-terminally to the BOX1 motif ($_{243}$IFPPVPGPK$_{251}$
237 (UNIPROT); $_{245}$PPVPGPK$_{251}$ (elm.eu.org)).
238
239 As the resonance-broadening precluded observation of the bound state, two overlapping peptides,
240 Pep1 (K235-D256) and Pep2 (K253-T280), were constructed and evaluated by CD spectroscopy. In
241 isolation, the peptides were disordered as judged by the negative ellipticity at 200 nm in their far-UV
242 CD spectra (***Figure 2G***). Pep1 and Pep2 were titrated with C_8-PI(4,5)P_2 and the structural changes
243 monitored (***Figure 2G***). For Pep2, the far-UV CD signal was unaffected by the presence of C_8-
244 PI(4,5)P_2. In contrast, for Pep1, large spectral changes were seen, which were unrelated to helix
245 formation. Subtracting the spectra in the presence and absence of C_8-PI(4,5)P_2, revealed a negative
246 ellipticity minimum at 218 nm, a strong indicator of β-strands, showing that when bound to C_8-
247 PI(4,5)P_2, a distinct extended (strand-like structure) signature was seen (***Figure 2G***). This suggests
248 that this region of LID1 changes its conformational properties upon binding to C_8-PI(4,5)P_2. We
249 evaluated the intrinsic helical propensities of the two ICD segments by exposure to high
250 trifluorethanol (TFE) concentrations. Here, Pep2 was readily able to form helical structure as
251 expected from the presence of two transient helices (Haxholm et al., 2015) (***Figure 2G, top***), whereas
252 Pep1 was not (***Figure 2G, bottom***).
253
254 In summary, LID1 of the PRLR-ICD interacts with PI(4,5)P_2,with the primary interaction site located
255 in the K235-S290 region. Headgroup interaction was dominantly located to the region K235-D256
256 constituting the ICJM and the BOX1 motif and this interaction induced the formation of a regional
257 extended structure in the PRLR-ICD.
258

LID1 has specific PI(4,5)P_2 contacts which drive PI(4,5)P_2 recruitment

To obtain a more detailed characterization of the behaviour of the disordered PRLR-ICD near lipid bilayers, as well as the effect of different anionic lipid headgroups in these, we turned to molecular simulations. Here, as explained above, we focused on the LID1 (K235-H300), alone and in context of TMD, and first placed a coarse-grained (CG) model of the TMD-$ICD_{F206-H300}$ in three different mixed-membrane systems. These contained an upper leaflet consisting of 100% POPC and lower leaflets composed of a 90:5:5 or 80:10:10 mixture of POPC:POPS:PI(4,5)P_2 (***Figure 3AB***) or a 70:30 molar ratio mixture of POPC:1-palmitoyl-2-oleoyl-sn-glycero-3-phospho-L-serine (POPS) (***Figure 3 – figure supplement 1EF***). Since the Martini forcefield may produce unrealistically collapsed disordered regions, increasing the strength of the protein-water interactions by 8–10% has provided satisfactory results when applied to the simulation of other disordered regions or multidomain proteins (Thomasen et al., 2022). Thus, the simulations were run using a modified version of the Martini3 forcefield with a 10% increase in the strength of the protein-water interactions. For comparison, similar simulations were performed using the Martini2 forcefield (***Figure 3 – figure supplement 1***).

We first analysed the dynamics of the LID1 during the simulations focusing on the pattern of protein-lipid contacts. Here, we measured the number of protein-lipid contacts focusing either on interactions between the protein and lipid headgroups or the protein and lipid acyl chains. In both cases we determined the fraction of the simulation time that the protein and different parts of the lipid were within 7Å of each other. In general, we observed that residues in the N-terminal part of the LID1 (K235 - D255), which includes the ICJM and BOX1, established contacts with the bilayer in all three membrane systems (***Figure 3A,B, Figure 3 – figure supplement 2***) Furthermore, a hydrophobic region rich in prolines (V240–P250) made consistent contacts with the acyl-chains and much more than to the headgroups, indicating penetration into the lower-leaflet. Similar behaviour has been reported with CG-MD simulations for the juxtamembrane region of other single-pass transmembrane receptors (Hedger et al., 2015b). For PRLR, the pattern of interaction was independent on the lipid composition, at least in terms of protein-POPC contacts, and the region interacting with the lipids was similar in all three membrane systems (***Figure 3A,B, Figure 3 – figure supplement 2***).

Although the extent and pattern of protein-lipid interactions appeared constant, a striking observation was made in both systems containing PI(4,5)P_2. Here, protein-lipid interactions between residues K235 and K253 and PI(4,5)P_2 were present during a large fraction (≥50%) of the simulations, despite PI(4,5)P_2 being present at only 5% or 10% of the total lipids (***Figures 3 – figure supplement 2***). This was also observed in simulations with the Martini2 forcefield, in which the LID1 promptly collapsed in a globular and unstructured coil (***Figure 3 – figure supplement 1***). This suggested that PI(4,5)P_2 spontaneously accumulated, or in other ways become concentrated around the TMD-$ICD_{F206-H300}$. The computed average density maps for PI(4,5)P_2 indeed showed that PI(4,5)P_2 formed a microdomain around the TMD (***Figure 3D***). The low frequency of contacts between the protein and POPS suggests that POPS did not accumulate or compete with PI(4,5)P_2 for binding to the TMD-$ICD_{F206-H300}$, further supporting the preference for PI(4,5)P_2 observed earlier (Haxholm et al., 2015).

Similar preference was also observed with 5% PI(4,5)P_2 (***Figure 3 – figure supplement 2***) as well as with Martini2 (***Figure 3 – figure supplement 2E-F***).

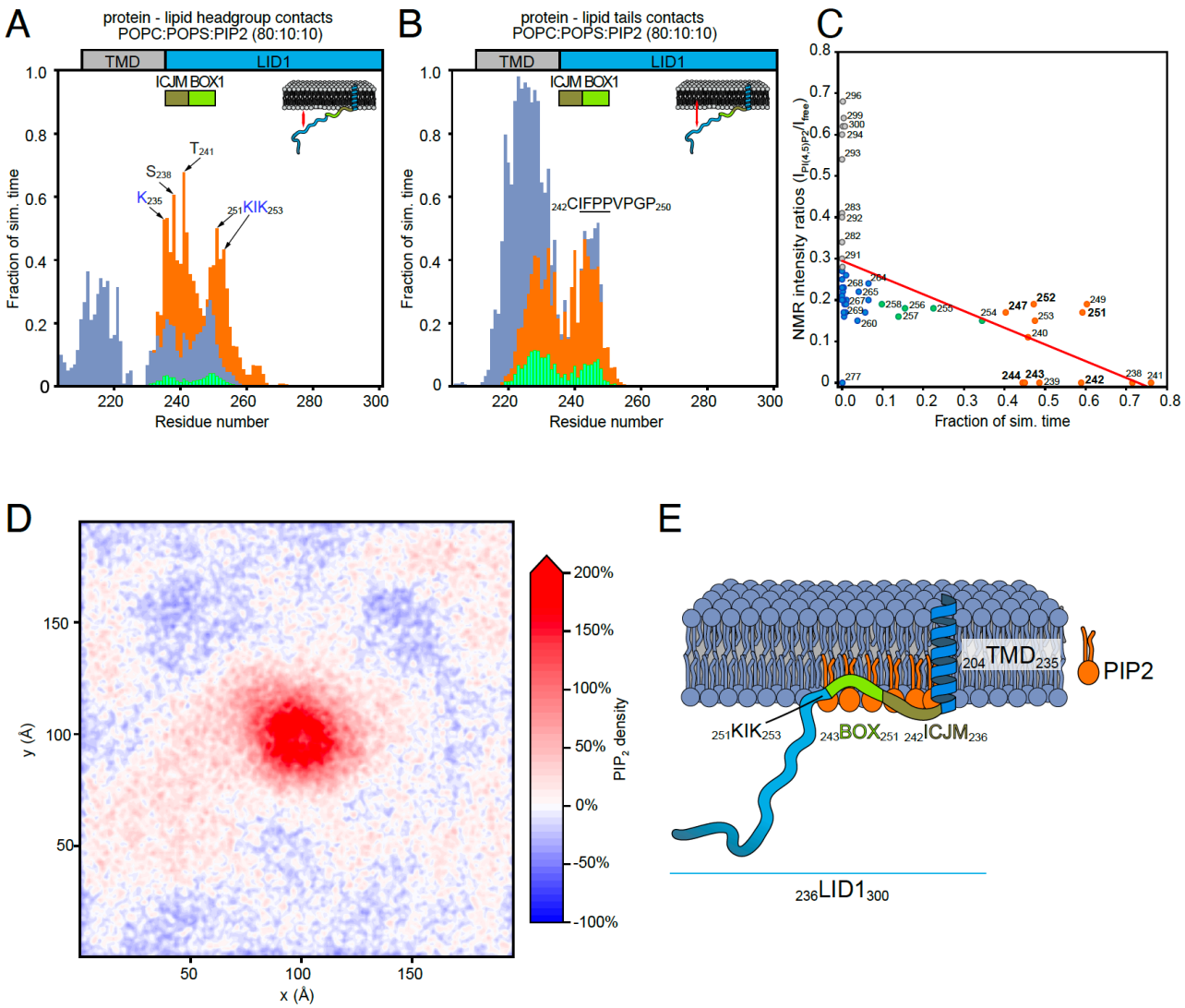

Fig. 3. Protein – lipid interactions of PRLR-ICD$_{LID1}$ obtained from CG-MD simulations. (A-B) Protein – lipid contact histograms for PRLR-ICD$_{LID1}$ + POPC:POPS:PI(4,5)P_2 (80:10:10). **A**) Contacts between the protein and lipid headgroups. A contact is counted if the distance between the backbone beads of the protein is ≤ 7 Å from the head-group beads of the lipids. **B**) Contacts between the protein and the acyl chains of the lipids. A contact is counted if the distance between the backbone bead of the protein is ≤ 7 Å from the acyl-chain bead of the lipids. **C**) Correlation between the change in NMR signal and the contact frequency between PRLR-ICD$_{LID1}$ and the lipid headgroups from the PRLR-ICD$_{LID1}$ + POPC:POPS:PI(4,5)P_2 (80:10:10) system. Pearson correlation coefficient of -0.55 with $p = 4.0\text{x}10^{-5}$ and R^2= 0.3. **D**) Average PI(4,5)P_2 density map (*xy*-plane) taken from the PRLR-ICD$_{LID1}$ + POPC:POPS:PI(4,5)P_2 (80:10:10) simulation. The map is colored according to the enrichment/depletion percentage with respect to the average density value. **E**) Schematic representation of how the interactions and the embedment into the membrane of PRLR contribute to the co-structure formation. The data from the simulations correspond to those of the production stage (see methods).

Figure supplement 1: *Protein – lipid interactions of PRLR-ICD$_{LID1}$ obtained from CG-MD simulations using the martini 3.0b3.2 forcefield*

Figure supplement 2: Complementary analysis of the Protein – lipid interactions of PRLR-ICD_{LID1} obtained from CG-MD simulations.

A more detailed analysis of LID1-PI(4,5)P_2 contacts revealed a preference for certain residues, shown as peaks in the protein-headgroup contact profiles. In particular K235, S238, T241, and K251 and K253, which define a KIK motif suggested as a PI(4,5)P_2 binding motif (Kjaergaard and Kragelund, 2017), engaged in highly populated contacts (***Figure 3A and figure supplement 2A***). The pattern of contacts was not affected by PI(4,5)P_2 concentration; however, the frequency of contacts almost doubled as a result of the increase from 5% to 10% of PI(4,5)P_2. The hydrophobic residues in the ICJM and BOX1 penetrate the headgroup layer and facilitate the approximation of the KIK motif to the PI(4,5)P_2 headgroups. The stabilization of the structure provided by the hydrophobic residues from the ICJM and BOX1 is also reflected in their decrease in flexibility, observed as a shoulder on the RMSF-BB plot, for the residues that comprise the ICJM and BOX1 of PRLR-LID1. Very similar profiles of the RMSF-BB plot was obtained for the systems with respectively 5 and 10% PI(4,5)P_2 in POPC:POPS, suggesting that the loss in flexibility is coupled to the buried hydrophobic residues rather than to specific PI(4,5)P_2 interaction (***Figure 3 – figure supplement 2C).*** Contributions from other positively charged residues such as K262 and K264 were very small. To validate the observations from the simulations, we compared the pattern of protein:PI(4,5)P_2 interactions observed in the NMR experiments to those from the simulations containing PI(4,5)P_2 (***Figure 3C***). A clear correlation between loss of NMR signal and high frequency of protein-PI(4,5)P_2 and POPC/POPS contacts in the 80:10:10 simulation was observed, reinforcing that the simulations are able to capture the specificity of protein-PI(4,5)P_2 interactions. Furthermore, both experiments (***Figure 2***) and simulations (***Figure 3***) show that the residues involved in binding to PI(4,5)P_2-containing membranes overlap with those that are involved in binding to JAK2.

In summary, the CG-simulations of TMD-$ICD_{F206-H300}$ near lipid membranes showed accumulation of PI(4,5)P_2 around the TMD and the N-terminus of LID1 involving the ICJM and BOX1. The residues made contact with the membrane independently of lipid type, with BOX1 residues acting as a tether by penetrating the headgroups. This tethering keeps positively charged residues, such as K251 and K253, near the membrane. This may be the driver for PI(4,5)P_2 recruitment, enhanced by higher PI(4,5)P_2 concentration. Intriguingly, we observed that the same regions involved in JAK2 binding (BOX1), also play roles in membrane association and lipid recruitment.

JAK2-FERM-SH2 and PRLR-ICD_{LID1} form co-structures with PI(4,5)P_2 on membranes

It has been suggested that JAK2 and PRLR interact constitutively in cells (Campbell et al., 1994; Rui et al., 1994) although recent data for the GHR have shown that the Src family kinase Lyn competes for this site (Chhabra et al., 2023). Thus, given our observations that residues from LID1 form lipid-specific contacts with the membrane constituents using the same region covering the binding interface with the FERM domain of JAK2, we decided to explore the structure and dynamics of the JAK2(FERM-SH2):PRLR(LID1) complex near lipid bilayers (***Figure 4***). To do so, an atomistic model of the complex of a smaller region of PRLR-$ICD_{K235-E284}$ bound to the JAK2-FERM-SH2 domains (residues P37 to T514) was built, taking advantage of crystal structures of JAK2-FERM-

361 SH2 and of JAK1-FERM-SH2 and TYK2-FERM-SH2 bound to analogous fragments of the ICDs of
362 the interferon λ- and α-receptors (IFNLR1 and IFNAR1), respectively. This model was used to
363 perform all-atom MD simulations in a water-box to obtain equilibrated structures for further
364 simulations, and to study the dynamics of the protein complex. The average contact map between
365 JAK2-FERM-SH2$_{P37-T514}$ and PRLR-ICD$_{K235-E284}$ showed clusters of contacts in which residues from
366 BOX1 of LID1 formed close contacts (avg. dist. ≤ 4Å) with residues from the F2 lobe (and the F1-
367 F2 linker) and the SH2 domain of JAK2-FERM-SH2, respectively (***Figure 4 – figure supplement***
368 ***1A***). C-terminally to BOX1, a second set of persistent contacts was observed, again involving charged
369 and hydrophobic residues including F255, L259, E261, K262 and K264 from PRLR-ICD$_{K235-E284}$.
370 Conservation analysis using ConSurf (Ashkenazy et al., 2016; Landau et al., 2005) (***Figure 4 – figure***
371 ***supplement 1B-D***) showed conserved residues in the interface, particularly those of BOX1 of PRLR
372 (P245, P248, K251, I252) (***Figure 4 – figure supplement 1B),*** while a patch of conserved residues
373 (T225, I229 and F236) in JAK2-FERM-SH2 formed close contact with residues from PRLR BOX1.
374 JAK2 residues V183 and L184 interacted with the backbone of $_{251}$KIK$_{253}$ of PRLR-ICD, whereas
375 other, less conserved residues such as E173 and E177 formed transient salt-bridges with K251 and
376 K253 of PRLR-ICD (see ***Figure 4 – figure supplement 1A)***. The contact map also showed that the
377 N-terminus of the ICJM remained flexible without close contacts with JAK2-FERM-SH2 (avg. dist.
378 ≥ 6Å).
379
380 Next, an equilibrated structure of the JAK2-FERM-SH2:PRLR-ICD$_{K235-E284}$ complex was used to
381 build a coarse-grained model, which was then placed near lipid bilayers of different lower leaflet
382 composition. A number of randomly positioned starting orientations were placed ~7 Å below the
383 lower leaflet (16 orientations for the POPC:POPS:PI(4,5)P_2 (80:10:10) membrane and eight for the
384 POPC:POPS (70:30) membrane). In addition we included twelve orientations of JAK-FERM-SH2
385 without the PRLR-ICD$_{K235-E284}$ placed near a POPC:POPS:PI(4,5)P_2 (80:10:10) membrane. For the
386 JAK2-FERM-SH2:PRLR-ICD$_{K235-E284}$ complex near a 70:30 POPC:POPS membrane, binding to the
387 lower leaflet was observed for only three of the eight systems (***Figure 4 – figure supplement 2A***). In
388 contrast, when PI(4,5)P_2 was present (10%), rapid binding of the complex to the membrane was
389 observed in all simulations reaching 97% saturation (***Figure 4 – figure supplement 2A***). Both
390 proteins in the complex showed specific clusters of residues with contacts to PI(4,5)P_2, POPS and
391 POPC, independent of the initial orientations (***Figure 4BC***). The number of contacts formed was
392 higher for the simulations with PI(4,5)P_2. This suggests that contacts with other components of the
393 membrane occur close to the bound PI(4,5)P_2. Overall, the PRLR-ICD $_{K235-E284}$ showed a pattern of
394 lipid contacts similar to the simulations of PRLR TMD-ICD$_{G204-H300}$ with the POPC:POPS:PI(4,5)P_2
395 (80:10:10) membrane (***Figure 4C***), with residues $K_{235}GY_{237}$contacting PI(4,5)P_2 headgroups for at
396 least 50% of the total contact time and with insertion into the membrane; note that this occurs even
397 though PRLR-ICD$_{K235-E284}$ is not tethered to the membrane via the TMD. Also, like in the PRLR
398 TMD-ICD$_{G204-H300}$ simulations, contacts made by C242 and I243 to POPC were still present. In
399 contrast, contacts by other residues from BOX1 and the KIK motif has lower populations. However,
400 and as expected from the location of the most frequent PRLR-ICD $_{K235-E284}$/lipid contacts, JAK2-
401 FERM-SH2 had more contacts in the F2 lobe of the FERM domain, mainly involving residues I223,
402 L224, R226, K227 and R230, constituting the regions where the N-terminus of PRLR-ICD$_{K235-E284}$ is

bound (***Figure 4B***). In the JAK2-FERM-SH2 simulations without PRLR-ICD and near a POPC:POPS:PI(4,5)P_2 (80:80:10) membrane, we observed that simulations initiated in eleven out of the twelve orientations ended up binding to the membrane (***Figure 4 – figure supplement 2A***). In this case, the overall binding pattern of protein-lipid contacts remained similar.

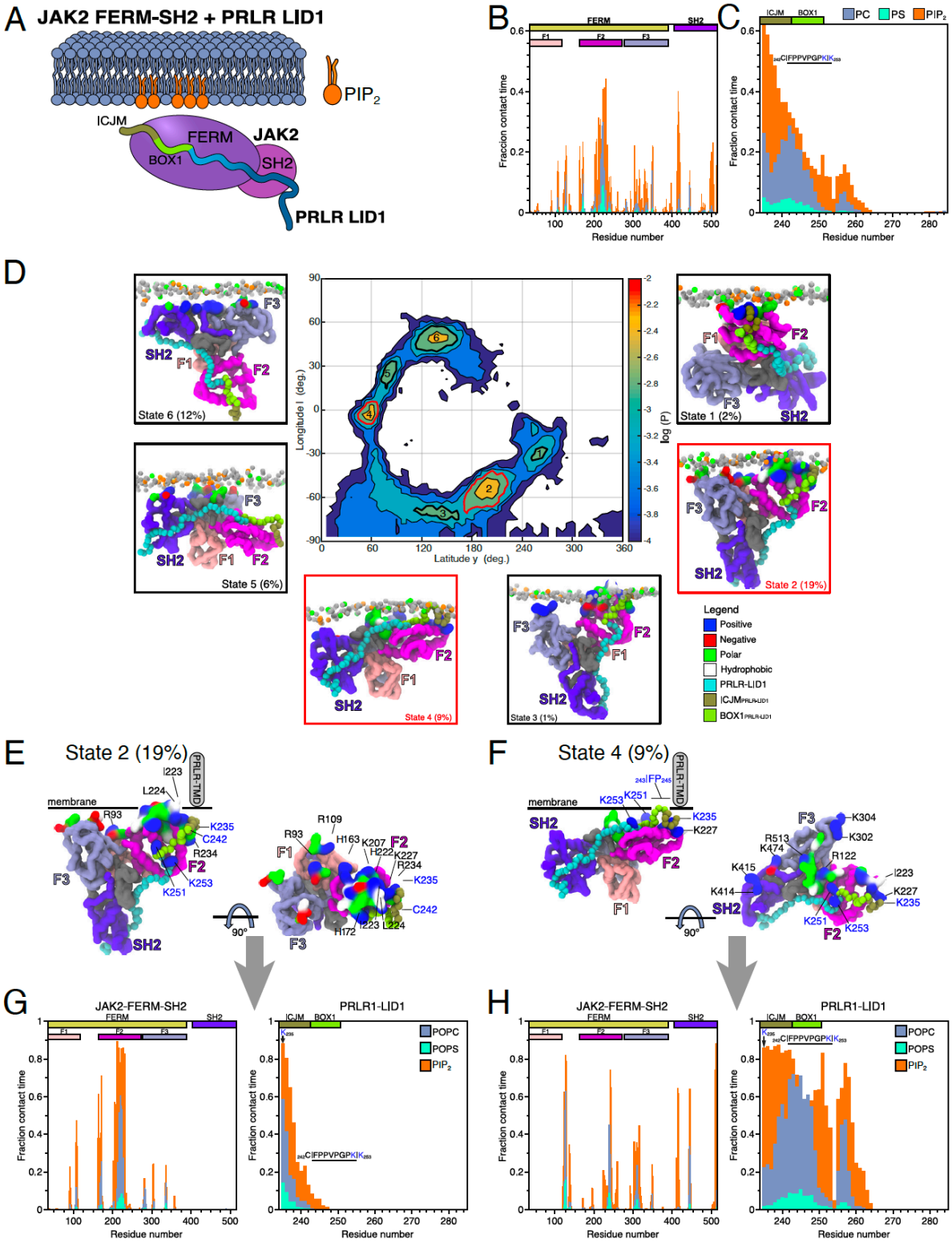

Fig. 4. Protein – lipid interactions of the JAK2-FERM-SH2 PRLR-ICD$_{LID1}$ complex obtained from CG-MD simulations. **A)** Schematic representation of the simulated system. Combined **B)** JAK2-FERM-SH2-lipid and **C)** PRLR-ICD$_{LID1}$-lipid contact frequency histograms for the 16 CG simulations of the JAK2-FERM-SH2 +PRLR-ICD$_{LID1}$+ POPC:POPS:PI(4,5)P_2 system. **D)** Distribution of the orientations adopted by the JAK2-FERM-SH2 + PRLR-ICD$_{LID1}$ complex when bound to lipids taken from the 16 simulations with POPC:POPS:PI(4,5)P_2 in the lower-leaflet. The snapshots surrounding the map correspond to representative conformations of the highlighted states also indicating the fraction total bound time for which each state was observed. Representative conformations of **E)** State 2 and **F)** State 4. The grey cylinder depicts the position where PRLR-TMD should be located. Representative protein-lipid contact histograms for **G)** State2 and **H)** State4 colored as in panels B and C.

Figure supplement 1: *Analysis of the JAK2-FERM-SH2- PRLR-ICD$_{LID1}$ AA-MD simulation***.**

Figure supplement 2. *Complementary analysis of Protein – lipid interactions of the JAK2-FERM-SH2 PRLR-ICD$_{LID1}$ complex obtained from CG-MD simulations*

Figure supplement 3. *Snapshots of the different binding states observed for the JAK2-FERM-SH2 – PRLR-ICD$_{LID1}$ complex with the complete structural model of JAK2*

Previous studies have suggested that the Martini2 forcefield model underestimates cation-π interactions between surface aromatic residues and choline headgroups on the membrane (Khan et al., 2020). However, this may not be applicable to other types of protein-membrane interactions, particularly where negatively charged headgroups are present. Our simulations involving PI(4,5)P_2) and POPS suggest that interactions between PRLR and the bilayer are primarily driven by positively charged residues in the protein, and that other protein-membrane interactions are secondary or occur between the lipids and residues that surround positively charged residues interacting with a PI(4,5)P_2 (or POPS) lipid. As a result, cation-π interactions may not be as important for the protein-lipid contact patterns we observed, but could be one explanation as to why we observe less frequent binding in the POPC:POPS systems.

In summary, our simulations showed that binding of JAK2 to the membrane was enhanced by the presence of PI(4,5)P_2 and that the ICD from PRLR and JAK2 formed a co-structure with PI(4,5)P_2 maintaining the contacts to the lipids observed for the individual proteins. The presence of PI(4,5)P_2 was essential for the membrane interactions.

The complex between JAK2-FERM-SH2 and LID1 shows preferential bound orientations with membranes containing PI(4,5)P_2

To characterize the membrane-bound modes of the complex in more detail, we took inspiration from Vogel *et al.* (Herzog et al., 2017) and constructed a map that represents the populations of different orientations of the JAK2-PRLR-ICD$_{K235-E284}$ complex relative to the membrane and extracted conformations to represent the most populated orientations as classified into states (***Figure 4D***). For the JAK2-PRLR-ICD$_{K235-E284}$ complex bound to the POPC:POPS:PI(4,5)P_2 (80:10:10) membrane, States 1–4 (~31% of the total contact time) showed the complex in an orientation where the N-terminus of PRLR-ICD$_{K235-E284}$ contacted and inserted into the bilayer similarly to what was observed in the PRLR TMD-ICD$_{G204-H300}$ simulations near a POPC:POPS:PI(4,5)P_2 bilayer. Of these four states, States 1, 2 and 3 had the F2 lobe of the JAK2-FERM domain and the ICJM region of PRLR-ICD$_{K235-E284}$ in contact with the membrane, penetrating below the headgroups, and acting as a pivot over which the protein-complex rotates, leaving the complex to hang as a "Y" from the membrane

453 (See ***Figure 4DE*** and ***MOVIE1***). State 4 on the other hand, while retaining the main contact points,
454 assumed a "flat" orientation with larger sections of the F2 lobe and F1-F2 linker from JAK2-FERM
455 and the entire N-terminal half of PRLR-ICD$_{K235-E284}$ (residues K235-G263) making a substantial
456 number of contacts with the membrane (***Figure 4DF*** and ***MOVIE2***). To examine whether the
457 identified states are compatible with functional states of the full-length kinase, we superimposed
458 representative conformations of States 1 to 6 with that of the full-length JAK2 model obtained from
459 the AlphaFold Protein Structure Database (UNIPROT O60674) (Jumper et al., 2021; Varadi et al.,
460 2022). This procedure revealed that both the Y (States 1, 2 and 3), and Flat (State 4) states keep the
461 other domains of JAK2 oriented towards the cytoplasmic space (***Figure 4 – figure supplement 3AD***),
462 supporting that these states could be functionally relevant. Furthermore, in the context of JAK2
463 dimerization required for signalling (Ferrao et al., 2018), these states allow for the correct orientation
464 for kinase domain dimerization. The two remaining states (States 5 and 6) showed an inverted
465 orientation in which the main protein-lipid interactions were formed by residues from the F3 lobe of
466 FERM and the SH2 domain, bringing the F2 lobe and the ICJM region of the PRLR-ICD
467 unrealistically far away from the membrane and from the connecting end of the TMD. Thus, States 5
468 and 6 appear functionally irrelevant, as further demonstrated by the superposition of the full-length
469 AlphaFold model of JAK2 in which the kinase domains would clash with the bilayer (***Figure 4 –***
470 ***figure supplement 3EF***).
471
472 **Different membrane co-structures have different exposures relevant to signalling**
473 We analysed the protein-lipid interactions formed by States 2 (Y) and 4 (Flat) in more detail, and
474 despite overall similar contact profiles, some key differences were observed (***Figure 4E–4H***). For
475 the Flat state, an increase in contacts was seen for residues K235 to L260 of PRLR-ICD$_{K235-E284}$ with
476 a pattern similar to the one observed in the PRLR-TMD-ICD$_{G204-H300}$ simulations with PI(4,5)P_2
477 present. Dominant PI(4,5)P_2 contacts were seen for K235–C242, followed by POPC contacts for
478 residues C242–P248, with a second PI(4,5)P_2 contact peak for K251 and a third around H257. For
479 the Y state, only residues K235–Y237 made substantial contacts with PI(4,5)P_2 and/or POPC, leaving
480 BOX1 and the KIK motif exposed to the solvent and making contacts with JAK2. For JAK2-FERM-
481 SH2, the main difference between the Y and Flat states was a large decrease in contacts to the F2
482 lobe in the Flat state accompanied by an increase in contacts in F3 and SH2. Residues in the F2 lobe
483 involved in homodimerization, orientation and activation, including L224, K227, R230 and R234
484 (Wilmes et al., 2020) were only accessible in the Y state, and not in the Flat state. Thus, we speculate
485 that the Y and Flat states may mimic functionally relevant conformations pertaining to active and
486 inactive states of the signalling complex. Mapping of residues that make contacts with the bilayer in
487 the two states to the conservation maps shows that several positively charged residues of JAK2-
488 FERM-SH2 are largely conserved. Particularly K207, R226, K227 and R228 in F2 with high
489 population contacts with PI(4,5)P_2 in the Y state are highly conserved. Similar conservation was seen
490 for the positively charged residues K235, K414, K415 and R513, that form contacts with PI(4,5)P_2 in
491 the Flat state.
492
493 Similar simulations were performed near a POPC:POPS 70:30 bilayer, which resulted in only one of
494 eight systems showing stable binding to the bilayer characterized by only one state (***Figure 4 – figure***

495 ***supplement 2A,B***). Here, residues from the F2 lobe of JAK2 form contacts with POPS lipids in a
496 narrow peak containing residues Q219 to R230, while for PRLR-ICD $_{K235-E284}$, residues from the
497 ICJM (K235-C242) and the BOX1 region (C242-P248), make high frequency contacts with both
498 POPS and POPC (***Figure 4 – figure supplement 2DE***). Overall this state is somewhat similar to State
499 3 observed for the simulations with PI(4,5)P_2. Similarly, for our simulations of JAK2-FERM-SH2
500 without PRLR near a bilayer with PI(4,5)P_2, 11 out of 12 stable binding conformations revealed three
501 most populated states (E1, E2, E3) (***Figure 4 – figure supplement 2C***). Characterization of these in
502 terms of protein-lipid contact profiles revealed that the positively charged residues in the F2 lobe play
503 an important role in binding to PI(4,5)P_2 in a similar manner as observed for the Y and Flat states of
504 the complex (***Figure 4 – figure supplement 2F***). Indeed, States 2 and 3 (***Figure4 – figure supplement***
505 ***2GH***) show remarkable similarities with the Flat and Y state from the simulations of the JAK2-
506 FERM-SH2:PRLR-ICD$_{K235-E284}$ complex near a similar bilayer.
507
508 Overall, the simulations highlight preferential binding of both JAK2-FERM-SH2, both alone and in
509 complex with PRLR-ICD$_{K235-E284}$ to PI(4,5)P_2, and show that the absence of this lipid decreases the
510 level of LID1 binding to the bilayer. Even in the absence of TMD tethering, the most populated bound
511 states recapitulate the binding mode observed for the PRLR-ICD alone. Another key observation is
512 the existence of different states in which different regions of both JAK2 FERM-SH2 domain and
513 LID1 of PRLR are exposed to the solvent or hidden below the bilayer.
514
515 **Key residues for membrane interaction control cellular signalling efficiency**
516 From the NMR experiments and MD simulations we identified residues in LID1 that interact with
517 different components of the membrane and/or the FERM-SH2 domain of JAK2. This resulted in four
518 clusters positioned in the ICJM (K235-C242), the BOX1 region (C242–P248), two basic patches of
519 the KxK motif type (K251–K253 and K262–K264) and hydrophobic residues in the region
520 connecting them, respectively. To decipher the specific role of these clusters for PI(4,5)P_2 interaction,
521 we introduced four sets of mutations in ICD$_{K235-G313}$ and investigated the effect on PI(4,5)P_2
522 interaction using NMR spectroscopy. Based on the NMR data and simulations, we focused on the
523 KxK motifs, which would be involved in binding to PI(4,5)P_2 (***Figure 3A***) and JAK2 (***Figure 4 –***
524 ***sumplement figure 1***), the CIF sequence, indicated to be important to membrane binding (***Figures 2***
525 ***and 3B***) and four hydrophobic residues, where at least two were seen to be important for JAK2
526 binding (***Figure 4- supplement figure 1***). We avoided interfering directly with the BOX1 core motif
527 (P245–P250) (Pezet et al., 1997). Thus, the CIF motif (C242–F244) was mutated to GAG (GAG
528 mutant: C242G, I243A, F244G), while the lysines in the KxK motifs (251–253 and 262–264) were
529 all mutated to either glycines (K4G mutant: K251G, K253G, K262G, K264G) or, for charge reversal,
530 to glutamates (K4E mutant: K251E, K253E, K262E, K264E). Finally, four hydrophobic residues
531 (I_{252}, F_{255}, L_{259} and L_{260}) were mutated to glycines (φ4G mutant). ^{15}N-PRLR-ICD$_{K235-G313}$ and the four
532 variants were titrated with up to 25× molar excess of C_8-PI(4,5)P_2, keeping the concentration below
533 the CMC. ^{1}H-^{15}N-HSQC spectra were recorded at each titration point and the changes in chemical
534 shifts and signal intensities were quantified (***Figure 5A***). Similarly to WT, all variants showed
535 negligible chemical shift changes (***Figure 5 – figure supplement 1***) but large peak intensity changes.
536 Decreased peak intensities were observed for all variants in the region of G236-D295, where the

537 changes were largest for the φ4G mutant and K4G, and similar to WT, while smaller effects were
538 seen for the GAG and the K4E variants, suggesting weaker affinities. Together, this indicates that the
539 KxK motifs and the CIF-motif are involved in PI(4,5)P_2 interaction, as expected from the contacts
540 predicted from simulation and NMR and CD data, yet none of these residues are essential for binding.
541

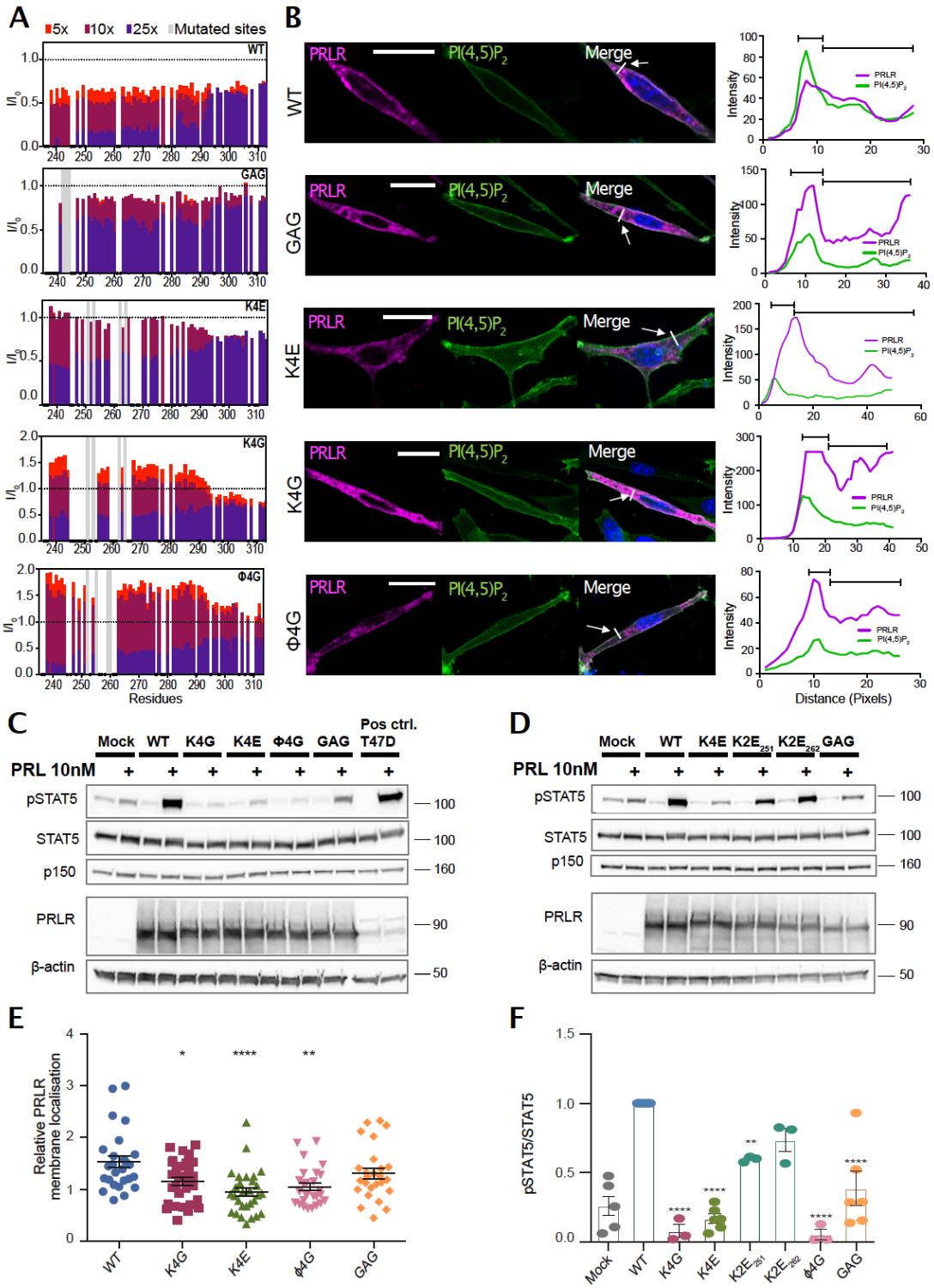

542

Fig. 5. PRLR variants with mutations in lipid interacting residues exhibit decreased PRL-stimulated STAT5 activation in AP1-2PH-PLCδ-GFP cells. A) NMR intensity changes of $ICD_{K235-G313}$ WT, K4G, K4E, φ4G and GAG variants upon titration with 5x, 10x and 25x molar excess C_8-PI(4,5)P_2 plotted against residue number. **B)** The PRLR variants (WT, K4G, K4E, φ4G, GAG) were transiently transfected in AP1 cells stably expressing the 2PH-PLCδ-GFP construct which visualizes the plasma membrane by binding PI(4,5)P_2. The cells were subsequently analysed by immunofluorescence microscopy, using antibodies against PRLR (magenta) and GFP (green), as well as DAPI (blue) to mark nuclei. To the right, examples of an average line-scan for each PRLR variant is shown. The fluorescence intensity depicted along the white line drawn (arrow) and green fluorescence (plasma membrane) was used to divide the line in a plasma membrane section and intracellular section, and relative membrane localization was calculated as the average fluorescence of PRLR in the membrane section divided by that in the intracellular section. **C, D)** AP1-2PH-PLCδ-GFP cells were transiently transfected with PRLR variants (WT, K4G, K4E, φ4G, GAG, $K2E_{253}$, $K2E_{261}$) and incubated overnight followed by serum starvation for 16-17 h and were subsequently incubated with or without 10 nM prolactin for 30 min. The resulting lysates were analysed by western blot for STAT5, pSTAT5 (Y964), PRLR, β-actin and p150 levels. The immunoblots are representative of three biological replicates. **E**) Ratio of plasma membrane localized receptor compared to intracellular receptor, analysed by line-scans as in B. Each point represents an individual cell, and data are based on three independent biological experiments per condition. Graphs show means with SEM error bars. *P<0.05, **P<0.01 and ****P<0.0001. One-way ANOVA compared to WT, unpaired**. F)** Quantification of western blot results shown as pSTAT5 normalized to total STAT5, relative to the WT condition. Graphs show means with SEM error bars. *P<0.05 and **P<0.01. One-way ANOVA compared to WT, unpaired.

Source file 1: Raw western blots (relating to *figure 5C*)

Source file 2: Raw western blot (relating to *figure 5D*)

Source file 3: Data summaries (relating to *figure 5E,F*)

Figure supplement 1: *Chemical shift perturbations of $ICD_{K235-G313}$ of A) WT, B) K4E, C) GAG, D) K4G and E) ϕ4G variants.*

Figure supplement 2: *^{15}N R_2 relaxation rates of $ICD_{K235-G313}$ of WT (grey bars), K4G (blue dots) and ϕ4G (red squares) variants.*

We observed dramatic increases in peak intensities for the K4G and φ4G variants in the presence of 5× and 10× molar excess of C_8-PI(4,5)P_2 when compared to WT (***Figure 5A***), suggesting changes in the dynamics of the chain. To adress this, we probed the backbone dynamics by acquiring ^{15}N R_2 relaxation rates of the WT, K4G and φ4G variants in the absence of C_8-PI(4,5)P_2 (***Figure 5 – figure supplement 2***). Compared to the WT, no major changes in R_2 were observed for two variants. The intensity increase observed for the K4G and φ4G variants during the titration with C_8-PI(4,5)P_2 therefore indicates increased backbone dynamics upon binding to C_8-PI(4,5)P_2 compared to the WT. Although we cannot explain this observation, it suggests that binding to C_8-PI(4,5)P_2 increases the dynamics of the first parts of the chain and thus require higher concentration of C_8-PI(4,5)P_2 to fully form the complex, as expected by the lower apparent affinity.

To address the implications of PI(4,5)P_2 interaction for PRLR membrane localization and downstream signalling, and to enable a potential separation of effect of perturbed membrane localization from direct PI(4,5)P_2 binding, we introduced the same four sets of mutations into the full-length PRLR. Together with WT PRLR, these were transiently transfected into AP1 mammalian epithelial cells, which were stably transfected with the fluorescent PI(4,5)P_2 reporter 2PH-PLCδ-GFP. The cells were subjected to fluorescence microscopy analysis of PRLR and the PI(4,5)P_2 reporter (Fig. 5B) and to western blot analysis of STAT5-activating phosphorylation (***Figures 5C-D, F-G***). None of the mutations fully abolished PRLR membrane localization. Western blot analysis

589 showed that the protein expression levels were similar for WT PRLR and all PRLR variants (***Figure***
590 ***5C***). However, compared to WT, the K4G, K4E and φ4G variants exhibited a significant reduction
591 in membrane localization as determined by line scan analysis (***Figures 5B,E***). This is in accordance
592 with their predicted JAK2 contacts obtained from the simulations, as JAK2 is known to be important
593 for PRLR trafficking (Huang et al., 2001). The PRL-induced STAT5 activation was significantly
594 decreased in cells expressing either the K4G, K4E or the φ4G variants, whereas STAT5 activation in
595 cells expressing the GAG variant was not significantly different from that of WT expressing cells
596 (***Figures 5C,F***). Decomposing the K4E variant into two individual mutants, in which only one of the
597 two KxK motifs was changed ($K2E_{251}$ and $K2E_{262}$) showed that the reduction in STAT5 activation
598 was attenuated in the variants with the individual mutations, compared to the drastic decrease
599 observed for the K4E mutant (***Figure 5D,G***). Thus, both KxK motifs are important for JAK/STAT
600 activation, which suggests that both $PI(4,5)P_2$ and JAK2 binding are important in this regard.
601
602 Taken together, these results show that while our data are consistent with the decreased membrane
603 localization contributing to the reduction of STAT5 activation, it is unlikely to account fully for the
604 effect observed for the K4G, K4E or the φ4G variants. Part of this reflects impaired binding to JAK2,
605 known to affect the amount of receptor at the cellular membrane. The MD simulations indicated that
606 only the first KxK motif is involved in lipid interaction while the second KxK motif is involved in
607 JAK2 interaction. Thus, a part of the the reduction in JAK/STAT activation in these variants could
608 arise from a combined effect of abolishing both $PI(4,5)P_2$- and JAK2 interaction within the LID1
609 region, which support the suggestion that co-structure formation between JAK2, PRLR and the
610 membrane is critical for optimal JAK/STAT signalling. However, within this co-structure, the
611 involved residues will likely affect several binding events, and thus separation of function by selective
612 mutations may not be straightforward.
613
614 **Discussion**
615 The sequence of the human PRLR has been known for more than 35 years (Boutin et al., 1988). Little
616 attention has, however, been given to the role of membrane composition for PRLR signalling, despite
617 it being placed in the plasma membrane where phosphoinositide levels are highly dynamic and
618 spatially variable, and being linked to cancer with lipid deregulation (Dadhich and Kapoor, 2022).
619 Here we asked if JAK2 and PRLR-ICD share a $PI(4,5)P_2$ binding site and if and how the binding to
620 $PI(4,5)P_2$ plays a role in the orientation of these proteins with respect to the membrane. Integrating
621 MD simulations with biophysical and cellular experiments has been critical in this endeavor. Our first
622 goal was to identify the residues of LID1 involved, as well as the structure formed—if any—in the
623 protein–lipid complex. Our results suggest that the residues that form the ICJM and BOX1 regions
624 of the ICD interact with the lipids via non-specific hydrophobic interactions that involve penetration
625 of the bilayer below the headgroups. This in turn enables positively charged residues of the $_{251}KIK_{253}$
626 motif to establish ionic interactions with $PI(4,5)P_2$ and in doing so the region folds into an extended
627 structure, similar to structures of other cytokine receptors in complex with either JAK1 or TYK2
628 (Wallweber et al., 2014; Zhang et al., 2016). In turn, $PI(4,5)P_2$ lipids accumulate around the TMD
629 and LID1 of PRLR, suggesting a relevant functional role of the interaction.
630

631 The results highlight the capacity of the LID1 to establish highly populated and specific interactions
632 with PI(4,5)P_2 via residues essential for its interaction with JAK2. Therefore, we addressed whether
633 LID1 in complex with the FERM-SH2 domain of JAK2 could engage with the lipid bilayer in the
634 absence of the TMD and with or without PI(4,5)P_2 lipids. Indeed, PI(4,5)P_2 was required for binding
635 of the complex to the membrane, as the presence of only POPS in the lower leaflet was not enough
636 to sustain binding despite its negative charge. Remarkably, when PI(4,5)P_2 was present, we observed
637 specific binding orientations that positioned the ICJM region of the LID1 in the same position as
638 when tethered to the TMD. Furthermore, in the complex, the protein-lipid contact profiles were
639 similar to the one observed for LID1 alone suggesting the PI(4,5)P_2 binding pattern to be maintained
640 in complex with JAK2. A detailed study of two of the most populated PRLR-bound states of JAK2
641 revealed a striking difference in orientation and contact pattern with the lipids, that could shed light
642 on functionally relevant states. For example, the most populated state, the Y state, had contacts from
643 the F2 lobe of the JAK2-FERM-SH2 domain and the ICJM of the PRLR, which penetrated the
644 membrane forming hydrophobic interactions with the acyl chains. In this orientation, regions of both
645 JAK2 and the PRLR that have been associated with receptor dimerization and activation for signaling
646 (Ferrao et al., 2018; Wilmes et al., 2020) are exposed to solvent and available for interactions. We
647 note that this orientation has resemblance to that shown in recent cryoEM structures of JAK1 bound
648 to IFNAR1 (Glassman et al., 2022). For the Flat state, we observed a drastic change in the protein-
649 lipid contact profiles for both proteins, but more markedly for LID1. While the main interaction site
650 remains the F2 lobe of JAK2 and the ICJM of the PRLR, the N-terminal residues of the LID1 now
651 lie sandwiched between the membrane and JAK2-FERM-SH2 domain and recapitulates the binding
652 pattern observed from TMD-$ICD_{F206-H300}$ simulations with membranes containing PI(4,5)P_2.
653 Remarkably, in this Flat state, most of the accessible regions in the Y states are now hidden under the
654 membrane. Thus, we speculate that the Y and Flat states may mimic an available and hidden state,
655 respectively, that could be relevant for regulation of dimerization and activation of signaling.
656 Interestingly, one residue that has been suggested to play a major role in JAK2 membrane association,
657 orientation, dimerization, and activation is L224 (Wilmes et al., 2020). This residue anchors into the
658 membrane only in the Y-state, and not in the Flat-state. Similarly, in simulations where L224 was
659 mutated to glutamate, a change in preferred orientation together with loss of dimerization and JAK2
660 and STAT5 phosphorylation was observed (Wilmes et al., 2020). This further highlight that the
661 orientation of the PRLR-JAK2 complex relative to the membrane has functional relevance.
662 Importantly, the presence of PI(4,5)P_2 in the membrane structurally tightens the path from the ECD,
663 folding the ICJM and BOX1 in an extended structure, making transmission of information of
664 hormone binding possible. Thus, signal relay by disordered linker of the PRLR can now be possible
665 through its complex formation with the membrane and JAK2 (***Figure 6***).
666

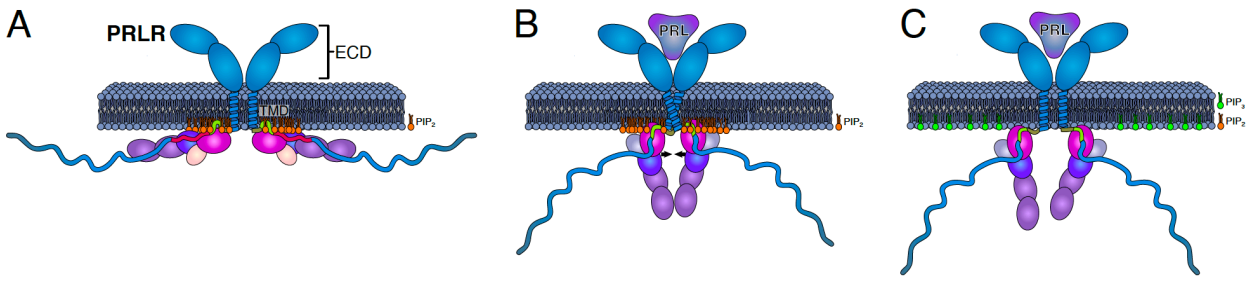

Fig. 6. Model of how co-structure formation between JAK2, PRLR and PI4(4,5)P_2 may contribute to signalling fidelity. The suggested states in signalling would be **A**) the inactive state of the co-structure exemplified by the Flat orientation. **B**) The hormone bound state exemplified by the co-structure in the Y orientation. **C**) Phosphorylation of PIP(4,5)P_2 to PI(3,4,5)P_3 for which the PRLR has no affinity may lead to downregulation and/or termination of signalling. The colour scheme of the proteins is identical to Fig.4.

Lastly, we tested the functional relevance of our observations by mutating residues that appeared significant for PI(4,5)P_2:PRLR:JAK2 co-structure formation and determining their impact on cellular PRL signaling. Both KxK motifs and the hydrophobic residues connecting them were important for PI(4,5)P_2 interaction, PRLR membrane localization and cellular JAK2/STAT5 signaling. From the MD simulation it was however evident that not all residues in these motifs were in direct contact with the membrane, further highlighting that co-structure formation between PRLR, JAK2 and the membrane is essential for optimal signal transduction. Another interesting observation was that even though mutating the CIF motif had the largest impact on PI(4,5)P_2 binding, it had only a limited effect on cellular JAK2/STAT5 signaling. Since the NMR results suggested that the ICJM serves as a primary PI(4,5)P_2 anchoring point facilitating additional contacts along the chain, this could indicate that a cooperative interaction within the co-structure is needed to control signaling and that PI(4,5)P_2 interaction is necessary for proper and substantial co-structure formation.

The PI(4,5)P_2-specific interactions observed point toward a possible regulatory role of PI(4,5)P_2 in PRLR signaling. Our simulations showed that the membrane embedded TMD-$ICD_{F206\text{-}H300}$ was associated with an accumulation of PI(4,5)P_2 around the TMD. One of the suggested roles of PI(4,5)P_2 as a regulatory lipid is indeed to form microdomains around proteins and reduce their lateral movement (Trimble and Grinstein, 2015; van den Bogaart et al., 2011). Another possible role can be inferred from previous studies on the EGFR. Evidence suggests a positive feedback loop where inhibition is released upon activation, because PI(4,5)P_2 is hydrolyzed to DAG and IP_3 by PLC_y (Maeda et al., 2018; McLaughlin et al., 2005). Specifically, we have previously shown that PRLR does not interact with PI(3,4,5)P_3 (Haxholm et al., 2015). As PI(4,5)P_2 is phosphorylated by the PI3-kinase to PI(3,4,5)P_3 during PRLR signaling (Aksamitiene et al., 2011; Yamauchi et al., 1998), this could indicate a way of attenuating signaling. Whether hydrolysis of PI(4,5)P_2 by PLC_y is relevant for PRLR signaling is not known.

Conclusions

Signal transduction by single-pass receptors through the membrane is still an enigma. In the present work we identify co-structure formation of the disordered LID1 of the PRLR, the membrane

703 constituent PI(4,5)P_2 and the FERM-SH2 domain of the JAK2, and demonstrate its importance for
704 PRLR signalling. This co-structure has at least two orientations, a Y-shaped state extending from the
705 membrane and a Flat-state with sites hidden in the membrane, the functional roles of which await
706 further elucidation. The co-structure led to accumulation of PI(4,5)P_2 at the TMD interface and
707 mutation of residues identified to specifically interact with PI(4,5)P_2 negatively affected PRL-
708 induced STAT5 activation. Facilitated by the co-structure, the disordered ICJM folds into an extended
709 structure, tightening the path from the ECD to the ICD. We suggest that the co-structure formed
710 between receptor, kinase and PI(4,5)P_2 is critical for signal relay from the extracellular to the
711 intracellular side of the membrane, and that different orientations of the co-structure exist that may
712 represent inactive and active states.
713
714 **Materials and Methods**
715 **Expression and purification of TMD $_{F206-V240}$, TMD-ICD $_{F206-S270}$ and ICD$_{G236-Q396}$**
716 PRLR-ICD$_{G236-Q396}$ was produced as described in (Haxholm et al., 2015), and TMD$_{F206-V240}$ and
717 TMD-ICD$_{F206-S270}$ were produced as described in (Bugge et al., 2015).
718
719 **Expression and purification of ICD$_{K235-G313}$ and variants (K4E, K4G, ϕ4G and GAG)**
720 ICD$_{K235-G313}$ and variants hereof, K4E (K251E, K253E, K262E, K264E), K4G (K251G, K253G,
721 K262G, K264G), ϕ4G (I252G; F255G, L259G, L260G) and GAG (C242G, I243A, F244G) were all
722 produced as follows: Competent BL21(DE3) were transformed using heat shock transformation with
723 pET24a+ plasmids encoding the protein of interest with N-terminal His$_6$-SUMO tag. One colony
724 was used to inoculate 10 mL of LB media with 50 µg/mL Kanamycin and incubated overnight at 37
725 °C at 160 RPM. The overnight culture was used to inoculate 1L M9 minimal media (3 g/l KH_2PO_4,
726 7.5 g/l Na_2HPO_4, 5 g/l NaCl, 1 mM $MgSO_4$, 4 g/l glucose, 1 g $^{15}NH_4Cl_2$, 1ml M2 trace solution, 50
727 µg/mL Kanamycin) and grown at 37 °C. At OD600 ~0.6 recombinant protein expression was induced
728 with 0.1 mM IPTG for 4H at 37 °C. Cells were harvested by centrifugation (5000xg, 20 min, 4°C)
729 and kept at -20 °C until purification. Cells were resuspended in 35 mL Buffer A (10 mM imidazole,
730 50 mM Tris (pH 8), 150 mM NaCl, 2 mM dithiothreitol (DTT) and lysed with French press at 25
731 kpsi, followed by centrifugation at 20.000xg, 45 min, 4 °C. The supernatant was applied to 5 mL of
732 pre-equilibrated Ni-NTA beads and incubated for 15 min followed by 50 mL wash with Buffer B 10
733 mM Imidazole, 50 mM Tris (pH 8), 1M NaCl, 2mM DTT) and 50 mL wash with Buffer A. Protein
734 was eluted with 10 mL Buffer C (250 mM Imidazole, 50 mM Tris (pH 8), 150 mM NaCl, 2 mM
735 DTT). The elution was supplemented with 0.01 mg ULP-1 and dialysed against 1 L of dialysis buffer
736 (50 mM Tris (pH 8), 150 mM NaCl, 1 mM DTT) overnight at 4 °C. The sample was re-applied to the
737 Ni-NTA column and incubated for 15 min. Flow through containing cleaved protein was collected,
738 and the remaining protein was eluted with 10 mL Buffer C. The sample was supplemented with 10
739 mM DTT before heating at 75 °C for 5 min with gentle rotation of the sample throughout. Sample
740 was transferred directly to ice for 10-15 min incubation followed by centrifugation at 20.000xg, 10
741 min, 4 °C. The supernatant was concentrated and supplemented with 5 mM betamercaptoenthaonl
742 (b-ME) before application to a HiLoad 16/60 Superdex75 prep grade column equilibrated in 20 mM

743 Na_2HPO_4/NaH_2PO_4, 150 mM NaCl, 5 mM b-ME (pH 7.3). Fractions containing pure protein were
744 pooled and concentrated
745
746 **CD spectroscopy**
747 The peptides covering residues K235-D256 (Pep1) and K253-T280 (Pep2), respectively were
748 purchased from KJ Ross (DK) at 95% purity from HPLC purification. The peptides were dissolved
749 in 10 mM Na_2HPO4/Na_2HPO4, pH 7.3 to a final concentration of 40 µM (Pep1) and 25 µM (Pep2)
750 and titrated with TFE or C_8-PI(4,5)P_2. The spectra were recorded in a 1mm Quartz cuvette on a Jasco-
751 810 spectropolarimeter purged with 8 l/min N_2 at 25 °C. A total of 10 accumulations were acquired
752 from 260-190 nm with the following settings: 0.5 nm data pitch, 1 nm band width, response time of
753 2 seconds, scanning speed of 10 nm/min. A background reference was recorded at identical settings
754 for each sample and subtracted from the relevant spectrum. The spectra were processed by fast
755 Fourier transform filtering and ellipticity converted to mean residual ellipticity ($[\theta]_{MRW}$)
756
757 **NMR spectroscopy**
758 *TMD* $_{F206-V240}$ *and TMD-ICD* $_{F206-S270}$
759 ^{15}N-labelled or $^{13}C,^{15}N$-labeled TMD-ICD$_{F206-S270}$ was solubilized in molar excess 1,2-dihexanoyl-
760 sn-glycero-3-phosphocholine (DHPC) dissolved in 50 mM NaCl, 20 mM Na_2HPO_4/NaH_2PO4 buffer,
761 pH 7.2. Subsequently, the DHPC embedded TMD-ICD$_{F206-S270}$ was subjected to thorough buffer
762 exchange in a 3 kDa cutoff spinfilter to remove residuals. For reconstitution into POPC SUVs, ^{15}N-
763 labeled TMD-ICD$_{F206-S270}$ was solubilized in 300 µL 5:1 methanol:chloroform and mixed with molar
764 excess POPC dissolved in chloroform. The constituents were mixed, followed by evaporation of the
765 organic solvent under a stream of N_2. When the lipid film appeared dry, it was either left under a
766 stream of N_2 or placed under vacuum for at least an hour. The resulting proteoliposome film was
767 rehydrated with 1 mL of 50 mM NaCl, 20 mM Na_2HPO_4/NaH_2PO_4 buffer, pH 7.2, followed by
768 extensive dialysis against the buffer in a 3.5 kDa MWCO dialysis tube at 4 °C. Subsequently, the
769 proteoliposome solution was sonicated in an ultrasonication bath or, if the solution did not clarify,
770 with an UP400S Ultrasonic Processor, in rounds of 2 s with 30 s rest between runs. Finally, the sample
771 was concentrated in a 3 kDa cutoff spinfilter.
772 All NMR samples of ^{15}N-labelled or $^{13}C,^{15}N$-labelled TMD-ICD$_{F206-S270}$ were added 10% (v/v)
773 D_2O, 2 mM tris(2-carboxyethyl)phosphine (TCEP), 1 mM sodium trimethylsilylpropanesulfonate
774 (DSS), 0.05% (v/v) NaN_3, and 50 mM NaCl, 20 mM Na_2HPO_4/NaH_2PO4 buffer (pH 7.2) to a final
775 volume of 370 µL followed by pH-adjustment to 7.2 (if needed). All spectra were acquired at 37 °C
776 because the peak intensities of the TMD region decreased at lower temperatures. Free induction
777 decays were transformed and visualized in NMRPipe (F Delaglio et al., 1995) and analysed using the
778 CcpNmr Analysis software (Vranken et al., 2005). Proton chemical shifts were referenced internally
779 to DSS at 0.00 ppm, with heteronuclei referenced by relative gyromagnetic ratios. For assignments
780 of backbone nuclei, heteronuclear NMR spectra of a sample containing 0.5 mM $^{13}C,^{15}N$-labelled
781 TMD-ICD$_{F206-S270}$ in 500 times molar excess DHPC were acquired on a Bruker 750-MHz (^1H)
782 equipped with a cryoprobe. HNCACB and CBCA(CO)NH spectra were acquired with 32 and 40 of
783 transients, respectively, and 20% non-uniform sampling (Mayzel et al., 2014), and used for manual
784 backbone assignments. SCSs were calculated using random coil chemical shifts from (Kjaergaard et

785 al., 2011) (obtained by supplying primary structure, pH and temperature to the webtool
786 http://www1.bio.ku.dk/english/research/bms/research/sbinlab/groups/mak/randomcoil/script/),
787 which were subtracted from the assigned TMD-ICD $_{F206-S270}$ chemical shifts.
788 The $^{1}H,^{15}N$-HSQC spectrum of 0.4 mM ^{15}N-labelled TMD-ICD$_{F206-S270}$ in POPC SUVs (100 times
789 molar excess of POPC) was acquired on a Varian INOVA 750- MHz (^{1}H) spectrometer equipped
790 with a room temperature probe. The number of transients was 104.
791
792 *ICD$_{K235-G313}$*
793 ICD$_{K235-G313}$ and the four variants (K4E, K4G, phi4G and GAG) were dialyzed at 4 °C overnight
794 against 20 mM Na_2HPO_4/NaH_2PO_4 (pH 7.3), 150 mM NaCl. The samples of 50 µM protein were
795 added 1 mM TCEP, 0.25 mM DSS and 10% (v/v) D_2O and centrifuged at 20.000 xg, 4 °C for 10 min
796 and transferred to 5mm Shigemi BMS-3 tubes. All NMR experiments were recorded at 5 °C on a
797 Bruker Avance III 600 MHz (^{1}H) spectrometer equipped with cryogenic probe. Free induction decays
798 were transformed and processed in qMDD (Orekhov and Jaravine, 2011), phased in NMRDraw
799 (Frank Delaglio et al., 1995) and analysed in CcpNMR analysis software (Vranken et al., 2005).
800 Proton chemical shifts were referenced to DSS and nitrogen and carbon to their relative gyromagnetic
801 ratios. ^{1}H-^{15}N-HSQC experiments were acquired using non-uniform sampling (Mayzel et al., 2014)
802 and recorded on 50 µM ^{15}N-ICD$_{K235-G313}$ (or variants) in the absence and presence of 5x, 10x and 25x
803 molar excess of C_8-PI(4,5)P_2 (Avanti Lipids 850185).
804 Transverse ^{15}N relaxation rates (R_2) of ICD$_{K235-G313}$ and the two variants, K4G and φ4G, were
805 acquired on Bruker Avance III 600 MHz (^{1}H) spectrometer with varying relaxation delays of 0 ms,
806 33.92 ms, 67.84 ms, 135.68 ms, 169.6 ms, 203.52 ms, 271.36 ms and 339,2 ms, measured in triplicates
807 and peak intensities fitted to single-exponential decays.
808
809 **Cell lines and media**
810 AP1-2PH-PLCδ-GFP cells (From J. Snipper; vector from Addgene plasmid #35142) were grown in
811 Minimum Essential Medium Eagle (EMEM, Gibco) containing 10% Fetal Bovine Serum (Sigma
812 Aldrich), 1% penicillin/streptomycin (Sigma), and 1% L-glutamine (Sigma). Stable AP1 clones
813 expressing 2PH-PLCδ-GFP were grown in the same medium, containing 600 µg/mL geneticin
814 (Merck-Millipore) to maintain expression of 2PH-PLCδ-GFP. Cell lines were maintained at 37 °C
815 with 95% humidity and 5% CO_2 and were passaged by gentle trypsination for a maximum of 15
816 passages.
817
818 **Immunoblotting**
819 Cells were grown to ~80% confluence in 6-well plates, washed in ice-cold PBS, lysed in boiling lysis
820 buffer (1% SDS, 10 mM Tris–HCl, pH 7.5, with phosphatase inhibitors), boiled for 1 min, sonicated,
821 and centrifuged to clear debris. Identical amounts of protein (12 µg/well) diluted in NuPAGE LDS
822 sample buffer (Novex) with 50% 0.5M DTT were boiled for 5 min, separated on Bio-Rad 10% Tris-
823 Glycine gels, and transferred to nitrocellulose membranes using the Trans-Blot Turbo Transfer
824 system (Bio-Rad). Membranes were stained with Ponceau S to confirm equal loading, blocked for 1
825 h at 37 °C in blocking buffer (TBST, 5% nonfat dry milk), and incubated with the relevant primary
826 antibodies in blocking buffer overnight at 4°C. After washing in TBST (TBS + 0.1% Tween-20),

827 membranes were incubated with HRP-conjugated secondary antibodies (1:2000, Sigma), washed in
828 TBST, and visualized using ECL reagent (Bio-Rad). Protein bands were quantified by densitometry
829 using ImageJ software, and normalized to those of STAT5 and then to WT.
830
831 **Immunofluorescence analysis**
832 For immunofluorescence experiments, cells were grown on 12 mm round glass coverslips to ~80%
833 confluency and fixed in 2% PFA (30 min at RT). Coverslips were washed three times for 3 x 5 min
834 in PBS, permeabilized for 15 min (0.5% Triton X-100 in TBS), blocked for 30 min (5% BSA in
835 TBST), and incubated with primary antibody in TBST + 1% BSA at RT for 1.5 h. Coverslips were
836 again washed in TBST + 1% BSA, and incubated with AlexaFluor488 and AlexaFluor568 conjugated
837 secondary antibody (1:600 in TBS + 1% BSA) for 1.5 h. Finally, coverslips were incubated with
838 DAPI (1:1000) for 5 min to stain nuclei, washed in TBST, and mounted in N-propyl-gallate mounting
839 medium (2% w/v in PBS/glycerol). Cells were visualized using the Olympus IX83 microscope with
840 a Yokogawa spinning disc confocal unit, using a 60X/1.4 NA oil emersion objective. Image
841 adjustments were carried out using ImageJ software. Line scans were performed using the
842 ColorProfiler ImageJ software plugin.
843
844 **Primary antibodies**
845 PRLR (Santa Cruz #SC20992), STAT5 (Santa Cruz #SC835), pSTAT5 (Y964) (Cell Signaling
846 #CS4322), p150 (BD #BD610473), β-actin (Sigma Aldrich #A5441).
847
848 **Modelling of simulated proteins**
849 *PRLR TMD-LID1 on a lipid bilayer*
850 To build a model of the hPRLR-TMD-ICD-LID1region (G204 to H300) we used the MODELLER
851 interface of Chimera (Pettersen et al., 2004; Webb and Sali, 2016). The structure of hPRLR-TMD
852 (PDB 2N7I (Bugge et al., 2016a)) was used as template for the transmembrane helix (in this structure
853 the residue at position 204 (P) was mutated to a G thus, in our model position 204 corresponds to a
854 glycine) and due to the lack of structural templates for the ICD, it was modelled as a disordered coil.
855 This all-atom model was used to build coarse-grained simulation systems where the TMD was
856 embedded in different lipid bilayers composed of POPC in the upper leaflet and either: i) POPC:POPS
857 (70:30), ii) POPC:POPS:PI(4,5)P_2 (90:5:5) and iii) POPC:POPS:PI(4,5)P_2 (80:10:10) in the lower
858 leaflet using the CHARMM-GUI martini_maker module (Jo et al., 2008; Qi et al., 2015). The
859 resulting systems were built using the Martini 2.2 forcefield topology and were later adapted to the
860 Martini 3 (version m3.b3.2) (Souza and Marrink, 2020) topology using the martinize2.py tool. For
861 these systems, the PI(4,5)P_2 parameters were adapted from their Martini2.2 version by changing the
862 names of the beads to the Martini3 naming scheme using as example other available lipids. These
863 Martini3 PI(4,5)P_2 parameters are available in our github repository (see the Data Avaliability
864 section). Secondary structure restraints from the Martini forcefield were only applied to the TMD and
865 no harmonic bond restraints were defined in the building of these systems.
866
867 *All-atom models of JAK2-FERM-SH2 and its complex with PRLR-ICD$_{LID1}$*

To build the JAK2-FERM-SH2 + PRLR-ICD$_{K235-E284}$ complex the following structures where used: JAK1-FERM-SH2 + IFNLR1 (PDB 5L04 (Zhang et al., 2016)), TYK2-FERM-SH2 + IFNAR1 (PDB 4PO6 (Wallweber et al., 2014)) and JAK2-FERM-SH2 (PDB 4Z32 (McNally et al., 2016)). A structural alignment of the three FEMR-SH2 domains was performed with STAMP (Russell and Barton, 1992) using the Multiseq module (Roberts et al., 2006) of VMD (Humphrey et al., 1996). The model of PRLR-ICD$_{K235-E284}$ was generated with the MODELLER interface of Chimera using as template the aligned receptor-ICD regions present on the structures 5L04 and 4PO6. A total 200 models were generated, and the best in terms of its DOPE score (Shen and Sali, 2006) was selected for further use. This resulted in a model of PRLR-ICD$_{K235-E284}$ bound to JAK2-FEMR-SH2. By combining this model with chain A of PDB 4Z32, a structural model of the JAK2-FERM-SH2 + PRLR-ICD$_{K235-E284}$ complex was obtained. All-atom simulation systems were built for JAK2-FERM-SH2 and the JAK2-FERM-SH2+PRLR-ICD$_{K235-E284}$ complex model. The missing residues on the loop of F3 of JAK2-FERM-SH2 were completed using CHARMM-GUI pbd-reader module (Jo et al., 2014, 2008). Hydrogen atoms were automatically added to the protein using the psfgen plugin of VMD (Humphrey et al., 1996). Aspartate, glutamate, lysine, and arginine residues were charged, and histidine residues were neutral. Simulation boxes comprised of solvent and 150 mM NaCl were generated using the CHARMM-GUI solution-builder module (Jo et al., 2008; Lee et al., 2016) using CHARMM36m (Huang et al., 2017) parameters and topologies for the protein and the TIP3P water model for the solvent.

Coarsed-grained models of JAK2-FERM-SH2 and its complex with PRLR-ICD$_{LID1}$

To build coarse-grained models of JAK2-FERM-SH2 and complex between JAK2-FERM-SH2 and PRLR-ICD$_{K235-E284}$ complex, a conformation from their respective all-atom MD simulations of the complex was taken after 150 ns (see below). These conformations were used to generate a CG model using the martinize.py script. The Martini 2.2 forcefield (de Jong et al., 2013) was used and intramolecular elastic bonds were defined for JAK2-FERM-SH2 in both systems. To keep the complex formed and to avoid a "collapse" of the disordered PRLR-ICD$_{LID1}$, inter-molecular harmonic bonds were also defined between JAK-FERM-SH2 and PRLR-ICD$_{K235-E284}$ in the complex. In both cases, a force constant of 400 kJ mol^{-1} nm^{-2} and lower and upper elastic bond cut-offs of 5Å and 9Å, respectively were used.

Coarse-grained models of JAK2-FERM-SH2 and JAK2-FERM-SH2 + PRLR-ICD$_{LID1}$ near a lipid bilayer

The relaxed CG-model of the JAK2-FERM-SH2 + PRLR-ICD$_{LID1}$ complex or JAK2-FERM-SH2 alone (see below) was placed near (~ 7Å) pre-equilibrated lipid bilayers with wo different compositions: POPC on the upper leaflet and two differen compositions on the lower leaflet: i) POPC:POPS (70:30), and ii) POPC:POPS:PI(4,5)P_2 (80:10:10). The systems were solvated with water beads and 150 mM NaCl. A total of 16 initial orientations of the protein were generated by rotating the protein around the x or the y axis (with z being the normal of the membrane).

Molecular dynamics (MD) simulations

Coarse-grained MD simulations

910 Coarse-grained MD simulations were performed with Gromacs 2016 or 2018 using the Martini 2.2
911 force field (de Jong et al., 2013) or the open beta version of the Martini 3 (3.b3.2) force field (Souza
912 and Marrink, 2020). For the PRLR-TMD-ICD$_{K235-L284}$ simulations we increased the strength of
913 interactions between protein and water by 10% to avoid excessive compaction of the disordered
914 regions, as has been previously done for IDPs and multi-domain proteins (Kassem et al., 2021; Larsen
915 et al., 2020; Thomasen et al., 2022). Other simulation parameters, common to all the CG simulations
916 performed, were chosen following the recommendations in (de Jong et al., 2016). Briefly, a time step
917 of 20 fs was used, the Verlet cut-off scheme was used considering a buffer tolerance of 0.005 kJ/(mol
918 ps atom). The reaction-field method was used for Coulomb interactions with a cut-off of 11 Å and a
919 relative permittivity of ε_r = 15. For van der Waals' interactions, a cut-off of 11 Å was used. The
920 velocity rescaling thermostat was employed with a reference temperature of T = 310 K, with a
921 coupling constant of τ_T = 1 ps. For the equilibrations, the Berendsen barostat was employed (p = 1
922 bar, τ_p = 3 ps), whereas the production runs were performed with a Parrinello-Rahman barostat (p =
923 1 bar, τ_p = 12 ps). A semi-isotropic pressure coupling was used for all the systems that contained a
924 lipid bilayer. For all systems, an initial round of equilibration with decreasing constraints applied to
925 the protein beads and lipid beads was performed following the protocol provided by CHARMM-GUI
926 Martini maker module. For the PRLR-TMD-ICD$_{K235-L284}$ simulations, a total of 11 µs of
927 unconstrained MD were performed of which the first microsecond was considered as equilibration
928 and the last 10 µs as production and used for analysis. For the JAK2-FERM-SH2 and the complex
929 between JAK2-FERM-SH2 in solution, 1 µs of unconstrained simulation was performed. In the case
930 of JAK2-FERM-SH2 or the complex between JAK2-FERM-SH2 and PRLR-TMD-ICD$_{K235-L284}$ near
931 a lipid bilayer, an unconstrained run of 5 µs was performed for each system and the complete
932 trajectory considered for analysis.
933
934 *All-atom molecular dynamics simulations*
935 All-atom MD simulations were performed using GROMACS 2016 and 2018 (Abraham et al., 2015),
936 using the CHARMM36m force field (Huang et al., 2017) for proteins and the TIP3P model for water.
937 The initial system was minimized followed by position restrained simulation in two different phases,
938 NVT and NPT. A 150 ns run of unconstrained NPT equilibration was then performed. The Berendsen
939 thermostat was used for the constrained relaxation runs and the Nose-Hoover thermostat for the
940 production runs. In all cases, the temperature was 310 K. For the NPT simulations, the Berendsen
941 barostat was used during relaxations and the Parinello-Rahman barostat used in unconstrained
942 production runs. In all cases the target pressure was 1 atm. In all the simulations, the Verlet-cutoff
943 scheme was used with a 2 fs timestep. A cutoff of 12 Å with a switching function starting at 10 Å was
944 used for non-bonded interactions along with periodic boundary conditions. The Particle Mesh Ewald
945 method was used to compute long-range electrostatic forces. Hydrogen atoms were constrained using
946 the LINCS (Hess et al., 1997) algorithm.
947
948 *Trajectory analyses*
949 Analysis of the obtained trajectories was performed using VMD plugins, GROMACS analysis tools
950 and in-house prepared tcl and python scripts, available on github (see below). For the characterization
951 of the orientation of the JAK2-FERM-SH2+PRLR-ICD$_{K235-E284}$ complex with respect to the lipid

bilayer we used the geographical coordinate system with latitude and longitude devised by Herzog et al. (Herzog et al., 2017). Lipid densities were calculated with the Volmap plugin from VMD considering only the PO4 beads and a 1Å grid. Density plots are shown as an enrichment score with values representing the percentage of enrichment or depletion with respect to the average value on the system as done previously in (Corradi et al., 2018). All molecular renderings were done with VMD (Humphrey et al., 1996). Protein-protein contact maps were calculated using CONAN (Mercadante et al., 2018).

Acknowledgements

The authors thank the SYNERGY, BRAINSTRUC and REPIN consortia for valuable discussion and Signe A. Sjørup and Katrine Franklin Mark for skilled technical assistance. We are grateful to Dr. Julie Schnipper for generating the AP1-2PH-PLCδ-GFP cells and to Prof. Vincent Goffin for initial discussions regarding the importance of the KxK-motifs in PRLR.

Additional information

Funding

Funder	*Grant reference number*	*Author*
Novo Nordisk Foundation	NNF18OC0033926	Birthe B. Kragelund
Novo Nordisk Foundation	NNF15OC0016670	Birthe B. Kragelund, Stine F. Pedersen, Lise Arleth
Lundbeck Foundation	BRAINSTRUC	Kresten Lindorff-Larsen, Lise Arleth, Birthe B. Kragelund

The funders had no role in study design, data collection and interpretation, or the decision to submit the work for publication

Author contributions

Raul Araya-Secchi, Formal analysis, Validation, Investigation, Visualization, Methodology, Writing - original draft; **Katrine Bugge**, Formal analysis, Validation, Investigation, Visualization, Methodology, Writing - review and editing; **Pernille Seiffert,** Investigation, Visualization, Methodology, Writing - original draft, Writing - review and editing; **Amalie Petry**, Investigation; **Gitte W. Haxholm,** Investigation, **Kresten Lindorff-Larsen**, Validation, Supervision, Writing - review and editing, Funding; **Stine F. Pedersen**, Conceptualization, Resources, Formal analysis, Supervision, Funding acquisition, Writing - review and editing;; **Lise Arleth,** Conceptualization, Writing - review and editing; Resources, Formal analysis, Supervision, Funding acquisition; **Birthe B. Kragelund**, Conceptualization, Formal analysis, Validation, Resources, Formal analysis, Visualization, Supervision, Funding acquisition analysis, Writing - original draft, Writing - review and editing;

Author ORCIDs

Raul Araya-Secchi https://orcid.org/0000-0002-4872-3553
Katrine Bugge https://orcid.org/0000-0002-6286-6243
Pernille Seiffert https://orcid.org/0000-0003-4213-5336

Amalie Petry
Gitte W. Haxholm
Kresten Lindorff-Larsen https://orcid.org/0000-0002-4750-6039
Stine Falsig Pedersen https://orcid.org/0000-0002-3044-7714
Lise Arleth https://orcid.org/0000-0002-4694-4299
Birthe B. Kragelund https://orcid.org/0000-0002-7454-1761

Additional files

Supplementary files

MDAR checklist

Data availability

All data needed to evaluate the conclusions in the paper are present in the paper and/or the Supplementary Materials. The MD data and models together with the scripts used in the trajectory analysis are available on Github at https://github.com/Niels-Bohr-Institute-XNS-StructBiophys/PRLRmodel. NMR chemical shifts for the PRLR-ICD$_{G236-Q396}$ are deposited in the BioMagResBank under the accession number 51695.

REFERENCES

Abraham MJ, Murtola T, Schulz R, Páll S, Smith JC, Hess B, Lindahl E. 2015. GROMACS: High performance molecular simulations through multi-level parallelism from laptops to supercomputers. *SoftwareX* **1–2**:19–25. doi:10.1016/j.softx.2015.06.001

Aksamitiene E, Achanta S, Kolch W, Kholodenko BN, Hoek JB, Kiyatkin A. 2011. Prolactin-stimulated activation of ERK1 / 2 mitogen-activated protein kinases is controlled by PI3-kinase / Rac / PAK signaling pathway in breast cancer cells. *Cell Signal* **23**:1794–1805. doi:10.1016/j.cellsig.2011.06.014

Ashkenazy H, Abadi S, Martz E, Chay O, Mayrose I, Pupko T, Ben-Tal N. 2016. ConSurf 2016: an improved methodology to estimate and visualize evolutionary conservation in macromolecules. *Nucleic Acids Res* **44**:W344-50. doi:10.1093/nar/gkw408

Bachelot A, Binart N. 2007. Reproductive role of prolactin. *Reproduction* **133**:361–369. doi:10.1530/REP-06-0299

Basak S, Saikia N, Kwun D, Choi UB, Ding F, Bowen ME. 2022. Different Forms of Disorder in NMDA-Sensitive Glutamate Receptor Cytoplasmic Domains Are Associated with Differences in Condensate Formation. *Biomolecules* **13**. doi:10.3390/BIOM13010004

Bocharov E V., Lesovoy DM, Bocharova O V., Urban AS, Pavlov K V., Volynsky PE, Efremov RG, Arseniev AS. 2018. Structural basis of the signal transduction via transmembrane domain of the human growth hormone receptor. *Biochimica et Biophysica Acta (BBA) - General Subjects* **1862**:1410–1420. doi:10.1016/j.bbagen.2018.03.022

Bole-Feysot C, Goffin V, Edery M, Binart N, Kelly PA. 1998. Prolactin (PRL) and its receptor: actionm signal transduction pathways and phenotypes observed in PRL receptor knockout mice. *Endocr Rev* **19**:225–268.

1037 Bompard G, Martin M, Roy C, Vignon F, Freiss G. 2003. Membrane targeting of protein tyrosine
1038 phosphatase PTPL1 through its FERM domain via binding to phosphatidylinositol 4,5-
1039 biphosphate. *J Cell Sci* **116**:2519–30. doi:10.1242/jcs.00448
1040 Boutin JM, Jolicoeur C, Okamura H, Gagnon J, Edery M, Shirota M, Banville D, Dusanter-Fourt I,
1041 Djiane J, Kelly PA. 1988. Cloning and expression of the rat prolactin receptor, a member of
1042 the growth hormone/prolactin receptor gene family. *Cell* **53**:69–77. doi:10.1016/0092-
1043 8674(88)90488-6
1044 Brooks AJ, Dai W, O'Mara ML, Abankwa D, Chhabra Y, Pelekanos R a, Gardon O, Tunny K a,
1045 Blucher KM, Morton CJ, Parker MW, Sierecki E, Gambin Y, Gomez G a, Alexandrov K,
1046 Wilson I a, Doxastakis M, Mark AE, Waters MJ. 2014. Mechanism of Activation of Protein
1047 Kinase JAK2 by the Growth Hormone Receptor. *Science (1979)* **344**:1249783–1249783.
1048 doi:10.1126/science.1249783
1049 Brooks AJ, Dehkhoda F, Kragelund BB. 2016. Cytokine Receptors. *Principles of Endocrinology*
1050 *and Hormone Action*. doi:10.1007/978-3-319-27318-1
1051 Broutin I, Jomain J-B, Tallet E, van Agthoven J, Raynal B, Hoos S, Kragelund BB, Kelly P a,
1052 Ducruix A, England P, Goffin V. 2010. Crystal structure of an affinity-matured prolactin
1053 complexed to its dimerized receptor reveals the topology of hormone binding site 2. *J Biol*
1054 *Chem* **285**:8422–33. doi:10.1074/jbc.M109.089128
1055 Brown RJ, Adams JJ, Pelekanos RA, Wan Y, McKinstry WJ, Palethorpe K, Seeber RM, Monks
1056 TA, Eidne KA, Parker MW, Waters MJ. 2005. Model for growth hormone receptor activation
1057 based on subunit rotation within a receptor dimer. *Nat Struct Mol Biol* **12**:814–821.
1058 doi:10.1038/nsmb977
1059 Bugge K, Papaleo E, Haxholm GW, Hopper JTS, Robinson C v, Olsen JG, Lindorff-Larsen K,
1060 Kragelund BB. 2016. A combined computational and structural model of the full-length
1061 human prolactin receptor. *Nat Commun* **7**:11578. doi:10.1038/ncomms11578
1062 Bugge K, Steinocher H, Brooks AJ, Lindor K, Kragelund BB. 2015. Exploiting Hydrophobicity for
1063 Efficient Production of Transmembrane Helices for Structure Determination by NMR
1064 Spectroscopy. *Anal Chem* **87**:9126–9131. doi:10.1021/acs.analchem.5b02365
1065 Campbell GS, Argetsinger LS, Ihle JN, Kelly PA, Rillema JA, Carter-Su C. 1994. Activation of
1066 JAK2 tyrosine kinase by prolactin receptors in Nb2 cells and mouse mammary gland explants.
1067 *Proceedings of the National Academy of Sciences* **91**:5232–5236. doi:10.1073/pnas.91.12.5232
1068 Carracedo A, Pandolfi PP. 2008. The PTEN–PI3K pathway: of feedbacks and cross-talks.
1069 *Oncogene* **27**:5527–5541. doi:10.1038/onc.2008.247
1070 Chavent M, Karia D, Kalli AC, Domański J, Duncan AL, Hedger G, Stansfeld PJ, Seiradake E,
1071 Jones EY, Sansom MSP. 2018. Interactions of the EphA2 Kinase Domain with PIPs in
1072 Membranes: Implications for Receptor Function. *Structure* **26**:1025-1034.e2.
1073 doi:10.1016/J.STR.2018.05.003
1074 Chhabra Y, Seiffert P, Gormal RS, Vullings M, Lee CMM, Wallis TP, Dehkhoda F, Indrakumar S,
1075 Jacobsen NL, Lindorff-Larsen K, Durisic N, Waters MJ, Meunier FA, Kragelund BB, Brooks
1076 A. 2022. Tyrosine Kinases Compete for Growth Hormone Receptor Binding and Regulate
1077 Receptor Mobility and Degradation. *SSRN Electronic Journal*. doi:10.2139/ssrn.4260495
1078 Clevenger C v, Rui H. 2022. Breast Cancer and Prolactin – New Mechanisms and Models.
1079 *Endocrinology* **163**. doi:10.1210/endocr/bqac122
1080 Corradi V, Mendez-Villuendas E, Ingólfsson HI, Gu R-X, Siuda I, Melo MN, Moussatova A,
1081 DeGagné LJ, Sejdiu BI, Singh G, Wassenaar TA, Delgado Magnero K, Marrink SJ, Tieleman
1082 DP. 2018. Lipid–Protein Interactions Are Unique Fingerprints for Membrane Proteins. *ACS*
1083 *Cent Sci* **4**:709–717. doi:10.1021/acscentsci.8b00143

1084 Dadhich R, Kapoor S. 2022. Lipidomic and Membrane Mechanical Signatures in Triple-Negative
1085 Breast Cancer: Scope for Membrane-Based Theranostics. *Mol Cell Biochem*.
1086 doi:10.1007/s11010-022-04459-4
1087 de Jong DH, Baoukina S, Ingólfsson HI, Marrink SJ. 2016. Martini straight: Boosting performance
1088 using a shorter cutoff and GPUs. *Comput Phys Commun* **199**:1–7.
1089 doi:10.1016/j.cpc.2015.09.014
1090 de Jong DH, Singh G, Bennett WFD, Arnarez C, Wassenaar TA, Schäfer L V., Periole X, Tieleman
1091 DP, Marrink SJ. 2013. Improved Parameters for the Martini Coarse-Grained Protein Force
1092 Field. *J Chem Theory Comput* **9**:687–697. doi:10.1021/ct300646g
1093 de Vos AM, Ultsch M, Kossiakoff AA. 1992. Human growth hormone and extracellular domain of
1094 its receptor: crystal structure of the complex. *Science* **255**:306–12.
1095 Delaglio F, Grzesiek S, Vuister GW, Zhu G, Pfeifer J, Bax A. 1995. NMRPipe: a multidimensional
1096 spectral processing system based on UNIX pipes. *J Biomol NMR* **6**:277–93.
1097 Delaglio Frank, Grzesiek S, Vuister GW, Zhu G, Pfeifer J, Bax A. 1995. NMRPipe: A
1098 multidimensional spectral processing system based on UNIX pipes. *J Biomol NMR* **6**:277–293.
1099 doi:10.1007/BF00197809
1100 Feng J, Mertz B. 2015. Novel phosphotidylinositol 4,5-bisphosphate binding sites on focal adhesion
1101 kinase. *PLoS One* **10**:1–12. doi:10.1371/journal.pone.0132833
1102 Ferrao RD, Wallweber HJA, Lupardus PJ. 2018. Receptor-mediated dimerization of JAK2 FERM
1103 domains is required for JAK2 activation. *Elife* **7**:1–21.
1104 Gadd SL, Clevenger C v. 2006. Ligand-independent dimerization of the human prolactin receptor
1105 isoforms: functional implications. *Mol Endocrinol* **20**:2734–2746. doi:10.1210/me.2006-0114
1106 Glassman CR, Tsutsumi N, Saxton RA, Lupardus PJ, Jude KM, Christopher Garcia K. 2022.
1107 Structure of a Janus kinase cytokine receptor complex reveals the basis for dimeric activation.
1108 *Science* **376**. doi:10.1126/SCIENCE.ABN8933
1109 Goñi GM, Epifano C, Boskovic J, Camacho-Artacho M, Zhou J, Bronowska A, Martín MT, Eck
1110 MJ, Kremer L, Gräter F, Gervasio FL, Perez-Moreno M, Lietha D. 2014. Phosphatidylinositol
1111 4,5-bisphosphate triggers activation of focal adhesion kinase by inducing clustering and
1112 conformational changes. *Proc Natl Acad Sci U S A* **111**:E3177-86.
1113 doi:10.1073/pnas.1317022111
1114 Goretzki B, Weidemann C, McCray B, Schäfer SL, Jansen J, Tebbe F, Mitrovic S-A, Nöth J,
1115 Donahue JK, Jeffries CM, Steinchen W, Stengel F, Sumner CJ, Hummer G, Hellmich UA.
1116 2023. Crosstalk between regulatory elements in the disordered TRPV4 N-terminus modulates
1117 lipid-dependent channel activity. *bioRxiv*. doi:10.1101/2022.12.21.521430
1118 Hamada K, Shimizu T, Matsui T, Tsukita S, Hakoshima T. 2000. Structural basis of the membrane-
1119 targeting and unmasking mechanisms of the radixin FERM domain. *EMBO J* **19**:4449–62.
1120 doi:10.1093/emboj/19.17.4449
1121 Hannan FM, Elajnaf T, Vandenberg LN, Kennedy SH, Thakker R v. 2022. Hormonal regulation of
1122 mammary gland development and lactation. *Nat Rev Endocrinol*. doi:10.1038/s41574-022-
1123 00742-y
1124 Haxholm GW, Nikolajsen LF, Olsen JG, Fredsted J, Larsen FH, Goffin V, Pedersen SF, Brooks AJ,
1125 Waters MJ, Kragelund BB. 2015. Intrinsically disordered cytoplasmic domains of two
1126 cytokine receptors mediate conserved interactions with membranes. *Biochem J* **468**:495–506.
1127 doi:10.1042/BJ20141243
1128 Hedger G, Sansom MSP, Koldsø H. 2015a. The juxtamembrane regions of human receptor tyrosine
1129 kinases exhibit conserved interaction sites with anionic lipids. *Sci Rep* **5**:9198.
1130 doi:10.1038/srep09198

Hedger G, Sansom MSP, Koldsø H. 2015b. The juxtamembrane regions of human receptor tyrosine kinases exhibit conserved interaction sites with anionic lipids. *Sci Rep* **5**:9198. doi:10.1038/srep09198

Herzog FA, Braun L, Schoen I, Vogel V. 2017. Structural Insights How PIP2 Imposes Preferred Binding Orientations of FAK at Lipid Membranes. *J Phys Chem B* **121**:3523–3535. doi:10.1021/acs.jpcb.6b09349

Hess B, Bekker H, Berendsen HJC, Fraaije JGEM. 1997. LINCS: A linear constraint solver for molecular simulations. *J Comput Chem* **18**:1463–1472. doi:10.1002/(SICI)1096-987X(199709)18:12<1463::AID-JCC4>3.0.CO;2-H

Huang J, Rauscher S, Nawrocki G, Ran T, Feig M, de Groot BL, Grubmüller H, MacKerell AD. 2017. CHARMM36m: an improved force field for folded and intrinsically disordered proteins. *Nat Methods* **14**:71–73. doi:10.1038/nmeth.4067

Huang LJ shen, Constantinescu SN, Lodish HF. 2001. The N-terminal domain of Janus kinase 2 is required for Golgi processing and cell surface expression of erythropoietin receptor. *Mol Cell* **8**:1327–1338. doi:10.1016/S1097-2765(01)00401-4

Humphrey W, Dalke A, Schulten K. 1996. VMD: Visual molecular dynamics. *J Mol Graph* **14**:33–38. doi:10.1016/0263-7855(96)00018-5

Jo S, Cheng X, Islam SM, Huang L, Rui H, Zhu A, Lee HS, Qi Y, Han W, Vanommeslaeghe K, MacKerell AD, Roux B, Im W. 2014. CHARMM-GUI PDB Manipulator for Advanced Modeling and Simulations of Proteins Containing Nonstandard Residues. pp. 235–265. doi:10.1016/bs.apcsb.2014.06.002

Jo S, Kim T, Iyer VG, Im W. 2008. CHARMM-GUI: A web-based graphical user interface for CHARMM. *J Comput Chem* **29**:1859–1865. doi:10.1002/jcc.20945

Jumper J, Evans R, Pritzel A, Green T, Figurnov M, Ronneberger O, Tunyasuvunakool K, Bates R, Žídek A, Potapenko A, Bridgland A, Meyer C, Kohl SAA, Ballard AJ, Cowie A, Romera-Paredes B, Nikolov S, Jain R, Adler J, Back T, Petersen S, Reiman D, Clancy E, Zielinski M, Steinegger M, Pacholska M, Berghammer T, Bodenstein S, Silver D, Vinyals O, Senior AW, Kavukcuoglu K, Kohli P, Hassabis D. 2021. Highly accurate protein structure prediction with AlphaFold. *Nature* **596**:583–589. doi:10.1038/s41586-021-03819-2

Kassem N, Araya-Secchi R, Bugge K, Barclay A, Steinocher H, Khondker A, Wang Y, Lenard AJ, Bürck J, Sahin C, Ulrich AS, Landreh M, Pedersen MC, Rheinstädter MC, Pedersen PA, Lindorff-Larsen K, Arleth L, Kragelund BB. 2021. Order and disorder—An integrative structure of the full-length human growth hormone receptor. *Sci Adv* **7**:eabh3805. doi:10.1126/sciadv.abh3805

Khan HM, Souza PCT, Thallmair S, Barnoud J, De Vries AH, Marrink SJ, Reuter N. 2020. Capturing Choline-Aromatics Cation-π Interactions in the MARTINI Force Field. *J Chem Theory Comput* **16**:2550–2560. doi:10.1021/ACS.JCTC.9B01194

Kjaergaard M, Brander S, Poulsen FM. 2011. Random coil chemical shift for intrinsically disordered proteins: Effects of temperature and pH. *J Biomol NMR* **49**:139–149. doi:10.1007/s10858-011-9472-x

Kjaergaard M, Kragelund BB. 2017. Functions of intrinsic disorder in transmembrane proteins. *Cellular and Molecular Life Sciences* **74**:3205–3224. doi:10.1007/s00018-017-2562-5

Kubatzky KF, Ruan W, Gurezka R, Cohen J, Ketteler R, Watowich SS, Neumann D, Langosch D, Klingmüller U. 2001. Self assembly of the transmembrane domain promotes signal transduction through the erythropoietin receptor. *Current Biology* **11**:110–115. doi:10.1016/S0960-9822(01)00018-5

1177 Landau M, Mayrose I, Rosenberg Y, Glaser F, Martz E, Pupko T, Ben-Tal N. 2005. ConSurf 2005:
1178 the projection of evolutionary conservation scores of residues on protein structures. *Nucleic*
1179 *Acids Res* **33**:W299-302. doi:10.1093/nar/gki370
1180 Larsen AH, John LH, Sansom MSP, Corey RA. 2022. Specific interactions of peripheral membrane
1181 proteins with lipids: what can molecular simulations show us? *Biosci Rep* **42**.
1182 doi:10.1042/BSR20211406
1183 Larsen AH, Wang Y, Bottaro S, Grudinin S, Arleth L, Lindorff-Larsen K. 2020. Combining
1184 molecular dynamics simulations with small-angle X-ray and neutron scattering data to study
1185 multi-domain proteins in solution. *PLoS Comput Biol* **16**:e1007870.
1186 doi:10.1371/journal.pcbi.1007870
1187 Lee J, Cheng X, Swails JM, Yeom MS, Eastman PK, Lemkul JA, Wei S, Buckner J, Jeong JC, Qi
1188 Y, Jo S, Pande VS, Case DA, Brooks CL, MacKerell AD, Klauda JB, Im W. 2016.
1189 CHARMM-GUI Input Generator for NAMD, GROMACS, AMBER, OpenMM, and
1190 CHARMM/OpenMM Simulations Using the CHARMM36 Additive Force Field. *J Chem*
1191 *Theory Comput* **12**:405–413. doi:10.1021/acs.jctc.5b00935
1192 Lu J, Dong W, Hammond GR, Hong Y. 2022. Hypoxia controls plasma membrane targeting of
1193 polarity proteins by dynamic turnover of PI4P and PI(4,5)P2. *Elife* **11**.
1194 doi:10.7554/eLife.79582
1195 Maeda R, Sato T, Okamoto K, Yanagawa M, Sako Y. 2018. Lipid-Protein Interplay in Dimerization
1196 of Juxtamembrane Domains of Epidermal Growth Factor Receptor. *Biophys J* **114**:893–903.
1197 doi:10.1016/j.bpj.2017.12.029
1198 Mani T, Hennigan RF, Foster LA, Conrady DG, Herr AB, Ip W. 2011. FERM Domain
1199 Phosphoinositide Binding Targets Merlin to the Membrane and Is Essential for Its Growth-
1200 Suppressive Function. *Mol Cell Biol* **31**:1983–1996. doi:10.1128/MCB.00609-10
1201 Mayzel M, Rosenlo J, Orekhov VY. 2014. Time-resolved multidimensional NMR with non-
1202 uniform sampling. *J Biomol NMR* **58**:129–139. doi:10.1007/s10858-013-9811-1
1203 McLaughlin S, Smith SO, Hayman MJ, Murray D. 2005. An Electrostatic Engine Model for
1204 Autoinhibition and Activation of the Epidermal Growth Factor Receptor (EGFR/ErbB)
1205 Family. *Journal of General Physiology* **126**:41–53. doi:10.1085/jgp.200509274
1206 McLaughlin S, Wang J, Gambhir A, Murray D. 2002. PIP(2) and proteins: interactions,
1207 organization, and information flow. *Annu Rev Biophys Biomol Struct* **31**:151–75.
1208 doi:10.1146/annurev.biophys.31.082901.134259
1209 McNally R, Toms A V., Eck MJ. 2016. Crystal Structure of the FERM-SH2 Module of Human
1210 Jak2. *PLoS One* **11**:e0156218. doi:10.1371/journal.pone.0156218
1211 Mercadante D, Gräter F, Daday C. 2018. CONAN: A Tool to Decode Dynamical Information from
1212 Molecular Interaction Maps. *Biophys J* **114**:1267–1273. doi:10.1016/j.bpj.2018.01.033
1213 Metcalf DG, Moore DT, Wu Y, Kielec JM, Molnar K, Valentine KG, Wand AJ, Bennett JS,
1214 DeGrado WF. 2010. NMR analysis of the αIIbβ3 cytoplasmic interaction suggests a
1215 mechanism for integrin regulation. *Proceedings of the National Academy of Sciences*
1216 **107**:22481–22486. doi:10.1073/pnas.1015545107
1217 Morris R, Kershaw NJ, Babon JJ. 2018. The molecular details of cytokine signaling via the
1218 JAK/STAT pathway. *Protein Science* **27**:1984–2009. doi:10.1002/pro.3519
1219 Newey PJ, Gorvin CM, Cleland SJ, Willberg CB, Bridge M, Azharuddin M, Drummond RS, van
1220 der Merwe PA, Klenerman P, Bountra C, Thakker R v. 2013. Mutant Prolactin Receptor and
1221 Familial Hyperprolactinemia. *New England Journal of Medicine* **369**:2012–2020.
1222 doi:10.1056/NEJMoa1307557

1223 Orekhov VY, Jaravine VA. 2011. Analysis of non-uniformly sampled spectra with multi-
1224 dimensional decomposition. *Prog Nucl Magn Reson Spectrosc* **59**:271–292.
1225 doi:10.1016/j.pnmrs.2011.02.002
1226 Park MJ, Sheng R, Silkov A, Jung DJ, Wang ZG, Xin Y, Kim H, Thiagarajan-Rosenkranz P, Song
1227 S, Yoon Y, Nam W, Kim I, Kim E, Lee DG, Chen Y, Singaram I, Wang L, Jang MH, Hwang
1228 CS, Honig B, Ryu S, Lorieau J, Kim YM, Cho W. 2016. SH2 Domains Serve as Lipid-Binding
1229 Modules for pTyr-Signaling Proteins. *Mol Cell* **62**. doi:10.1016/j.molcel.2016.01.027
1230 Patwardhan P, Resh MD. 2010. Myristoylation and membrane binding regulate c-Src stability and
1231 kinase activity. *Mol Cell Biol* **30**:4094–4107. doi:10.1128/MCB.00246-10
1232 Pettersen EF, Goddard TD, Huang CC, Couch GS, Greenblatt DM, Meng EC, Ferrin TE. 2004.
1233 UCSF Chimera - A visualization system for exploratory research and analysis. *J Comput Chem*
1234 **25**:1605–1612. doi:10.1002/jcc.20084
1235 Pezet A, Buteau H, Kelly PA, Edery M. 1997. The last proline of Box 1 is essential for association
1236 with JAK2 and functional activation of the prolactin receptor. *Mol Cell Endocrinol* **129**:199–
1237 208. doi:10.1016/S0303-7207(97)00063-4
1238 Qi Y, Ingólfsson HI, Cheng X, Lee J, Marrink SJ, Im W. 2015. CHARMM-GUI Martini Maker for
1239 Coarse-Grained Simulations with the Martini Force Field. *J Chem Theory Comput* **11**:4486–
1240 4494. doi:10.1021/acs.jctc.5b00513
1241 Rawat A, Harishchandran A, Nagaraj R. 2013. Fatty acyl chain-dependent but charge-independent
1242 association of the SH4 domain of Lck with lipid membranes. *J Biosci* **38**:63–71.
1243 doi:10.1007/s12038-012-9288-1
1244 Rawat A, Nagaraj R. 2010. Determinants of membrane association in the SH4 domain of Fyn: roles
1245 of N-terminus myristoylation and side-chain thioacylation. *Biochim Biophys Acta* **1798**:1854–
1246 63. doi:10.1016/j.bbamem.2010.06.009
1247 Roberts E, Eargle J, Wright D, Luthey-Schulten Z. 2006. MultiSeq: unifying sequence and structure
1248 data for evolutionary analysis. *BMC Bioinformatics* **7**:382. doi:10.1186/1471-2105-7-382
1249 Rowlinson SW, Yoshizato H, Barclay JL, Brooks AJ, Behncken SN, Kerr LM, Millard K,
1250 Palethorpe K, Nielsen K, Clyde-Smith J, Hancock JF, Waters MJ. 2008. An agonist-induced
1251 conformational change in the growth hormone receptor determines the choice of signalling
1252 pathway. *Nat Cell Biol* **10**:740–7. doi:10.1038/ncb1737
1253 Rui H, Kirken RA, Farrar WL. 1994. Activation of receptor-associated tyrosine kinase JAK2 by
1254 prolactin. *J Biol Chem* **269**:5364–8.
1255 Russell RB, Barton GJ. 1992. Multiple protein sequence alignment from tertiary structure
1256 comparison: Assignment of global and residue confidence levels. *Proteins: Structure,*
1257 *Function, and Genetics* **14**:309–323. doi:10.1002/prot.340140216
1258 Sackmann-Sala L, Goffin V. 2015. Prolactin-Induced Prostate Tumorigenesis. pp. 221–242.
1259 doi:10.1007/978-3-319-12114-7_10
1260 Seiffert P, Bugge K, Nygaard M, Haxholm GW, Martinsen JH, Pedersen MN, Arleth L, Boomsma
1261 W, Kragelund BB. 2020a. Orchestration of signaling by structural disorder in class 1 cytokine
1262 receptors. *Cell Communication and Signaling* **18**. doi:10.1186/s12964-020-00626-6
1263 Seiffert P, Bugge K, Nygaard M, Haxholm GW, Martinsen JH, Pedersen MN, Arleth L, Boomsma
1264 W, Kragelund BB. 2020b. Orchestration of signaling by structural disorder in class 1 cytokine
1265 receptors. *Cell Communication and Signaling* **18**. doi:10.1186/s12964-020-00626-6
1266 Seubert N, Royer Y, Staerk J, Kubatzky KF, Moucadel V, Krishnakumar S, Smith SO,
1267 Constantinescu SN. 2003. Active and Inactive Orientations of the Transmembrane and
1268 Cytosolic Domains of the Erythropoietin Receptor Dimer. *Mol Cell* **12**:1239–1250.
1269 Shen M-Y, Sali A. 2006. Statistical potential for assessment and prediction of protein structures.
1270 *Protein Sci* **15**:2507–24. doi:10.1110/ps.062416606

Sheng R, Jung DJ, Silkov A, Kim H, Singaram I, Wang ZG, Xin Y, Kim E, Park MJ, Thiagarajan-Rosenkranz P, Smrt S, Honig B, Baek K, Ryu S, Lorieau J, Kim YM, Cho W. 2016. Lipids regulate Lck protein activity through their interactions with the Lck Src homology 2 domain. *Journal of Biological Chemistry* **291**:17639–17650. doi:10.1074/jbc.M116.720284

Souza PCT, Marrink SJS. 2020. Martini 3 - Open Beta-Release. *http://cgmartini.nl*.

Stefanski KM, Russell CM, Westerfield JM, Lamichhane R, Barrera FN. 2021. PIP2promotes conformation-specific dimerization of the EphA2 membrane region. *Journal of Biological Chemistry* **296**. doi:10.1074/jbc.RA120.016423

Suh BC, Hille B. 2005. Regulation of ion channels by phosphatidylinositol 4,5-bisphosphate. *Curr Opin Neurobiol* **15**:370–378. doi:10.1016/J.CONB.2005.05.005

Thomasen FE, Pesce F, Roesgaard MA, Tesei G, Lindorff-Larsen K. 2022. Improving Martini 3 for Disordered and Multidomain Proteins. *J Chem Theory Comput* **18**:2033–2041. doi:10.1021/acs.jctc.1c01042

Trimble WS, Grinstein S. 2015. Barriers to the free diffusion of proteins and lipids in the plasma membrane. *Journal of Cell Biology* **208**:259–271. doi:10.1083/jcb.201410071

van den Bogaart G, Meyenberg K, Risselada HJ, Amin H, Willig KI, Hubrich BE, Dier M, Hell SW, Grubmüller H, Diederichsen U, Jahn R. 2011. Membrane protein sequestering by ionic protein–lipid interactions. *Nature* **479**:552–555. doi:10.1038/nature10545

Varadi M, Anyango S, Deshpande M, Nair S, Natassia C, Yordanova G, Yuan D, Stroe O, Wood G, Laydon A, Žídek A, Green T, Tunyasuvunakool K, Petersen S, Jumper J, Clancy E, Green R, Vora A, Lutfi M, Figurnov M, Cowie A, Hobbs N, Kohli P, Kleywegt G, Birney E, Hassabis D, Velankar S. 2022. AlphaFold Protein Structure Database: massively expanding the structural coverage of protein-sequence space with high-accuracy models. *Nucleic Acids Res* **50**:D439–D444. doi:10.1093/nar/gkab1061

Vranken WF, Boucher W, Stevens TJ, Fogh RH, Pajon A, Llinas M, Ulrich EL, Markley JL, Ionides J, Laue ED. 2005. The CCPN data model for NMR spectroscopy: Development of a software pipeline. *Proteins: Structure, Function, and Bioinformatics* **59**:687–696. doi:10.1002/prot.20449

Wallweber HJA, Tam C, Franke Y, Starovasnik MA, Lupardus PJ. 2014. Structural basis of recognition of interferon-α receptor by tyrosine kinase 2. *Nat Struct Mol Biol* **21**:443–448. doi:10.1038/nsmb.2807

Webb B, Sali A. 2016. Comparative Protein Structure Modeling Using MODELLER. *Curr Protoc Bioinformatics* **54**. doi:10.1002/cpbi.3

Wilmes S, Hafer M, Vuorio J, Tucker JA, Winkelmann H, Löchte S, Stanly TA, Pulgar Prieto KD, Poojari C, Sharma V, Richter CP, Kurre R, Hubbard SR, Garcia KC, Moraga I, Vattulainen I, Hitchcock IS, Piehler J. 2020. Mechanism of homodimeric cytokine receptor activation and dysregulation by oncogenic mutations. *Science (1979)* **367**:643–652. doi:10.1126/science.aaw3242

Yamauchi T, Kaburagi Y, Ueki K, Tsuji Y, Stark GR, Kerr IM, Tsushima T, Akanuma Y, Komuro I, Tobe K, Yazaki Y, Kadowaki T. 1998. Growth Hormone and Prolactin Stimulate Tyrosine Phosphorylation of Insulin Receptor Substrate-1, -2, and -3, Their Association with p85 Phosphatidylinositol 3-Kinase (PI3-kinase), and Concomitantly PI3-kinase Activation via JAK2 Kinase. *Journal of Biological Chemistry* **273**:15719–15726. doi:10.1074/jbc.273.25.15719

Zhang D, Wlodawer A, Lubkowski J. 2016. Crystal Structure of a Complex of the Intracellular Domain of Interferon λ Receptor 1 (IFNLR1) and the FERM/SH2 Domains of Human JAK1. *J Mol Biol* **428**:4651–4668. doi:10.1016/j.jmb.2016.10.005

1319
1320 **FIGURE LEGENDS**
1321 **Fig. 1: Schematics of the PRLR:PRL:JAK2 complex in the membrane.** The PRLR is shown in
1322 light blue, the PRL as a dark blue triangle, the PRLR-ICD as a disordered chain and JAK2 in purple.
1323 The PI(4,5)P_2 lipid (PIP2) is shown in orange. The intracellular juxtamembrane (ICJM) region and
1324 BOX1 of PRLR-ICD are highlighted in green nuances, while the three LIDs as defined in Haxholm
1325 et al., (Haxholm et al., 2015) are highlighted in red. For simplicity only one of the two ICDs is shown
1326 associated with JAK2 via the BOX1 (green) and BOX2 (orange) motifs.
1327
1328 **Fig. 2: The ICJM region of the PRLR interacts with PI(4,5)P_2. A)** Overview of investigated PRLR
1329 variants. **B)** Secondary chemical shifts (SCSs) of TMD-$ICD_{F206-S270}$ reconstituted in DHPC micelles.
1330 **C)** Correlation plot of the SCSs of $ICD_{G236-Q396}$ plotted against those of TMD-$ICD_{F206-S270}$. **D)** ^{15}N,^{1}H-
1331 HSQC spectra of ^{15}N-$ICD_{K235-G313}$ titrated with 5x, 10x and 25x molar excess of C_8-PI(4,5)P_2. **E)**
1332 Structure of C_8-PI(4,5)P_2 . **F)** Backbone amide chemical shift perturbations (CSPs) and peak intensity
1333 changes upon addition of C_8-PI(4,5)P_2 to ^{15}N-$ICD_{K235-G313}$ plotted against residue number. **G) Top**:
1334 Far-UV CD spectra of Pep1 titrated with C_8-PI(4,5)P_2 or in 65% TFE. **Middle:** Far-UV CD spectra
1335 of Pep1 in the presence of 5x-38x C_8-PI(4,5)P_2 subtracted with the spectrum of Pep1 in the absence
1336 of C_8-PI(4,5)P_2. **Bottom**: Far-UV CD spectra of Pep2 titrated with C_8-PI(4,5)P_2 or in 65% TFE**.**
1337 **Figure supplement 1**: *^{15}N, ^{1}H-HSQC spectra of A) $TMD_{F206-V240}$ and TMD-$ICD_{F206-S270}$ in DHPC*
1338 *micelles, and (B) TMD-$ICD_{F206-S270}$ in POPC SUVs.*
1339 **Figure supplement 2**: *C^{α} secondary chemical shifts of $ICD_{G236-Q396}$*
1340
1341 **Fig. 3. Protein – lipid interactions of PRLR-ICD_{LID1} obtained from CG-MD simulations. (A-**
1342 **B)** Protein – lipids contact histograms for PRLR-ICD_{LID1}+POPC:POPS:PI(4,5)P_2 (80:10:10). **A**)
1343 Contacts between the protein and lipid headgroups. A contact is counted if the distance between the
1344 backbone beads of the protein is ≤ 7 Å from the head-group beads of the lipids. **B**) Contacts between
1345 the protein and the acyl chains of the lipids. A contact is counted if the distance between the backbone
1346 bead of the protein is ≤ 7 Å from the acyl-chain bead of the lipids. **C**) Correlation between the change
1347 in NMR signal and the contact frequency between PRLR-ICD_{LID1} and the lipid headgroups from the
1348 PRLR-ICD_{LID1} + POPC:POPS:PI(4,5)P_2 (80:10:10) system. Pearson correlation coefficient of -0.55
1349 with $p = 4.0\text{x}10^{-5}$ and R^2= 0.3. **D**) Average PI(4,5)P_2 density map (*xy*-plane) taken from the PRLR-
1350 ICD_{LID1} + POPC:POPS:PI(4,5)P_2 (80:10:10) simulation. The map is colored according to the
1351 enrichment/depletion percentage with respect to the average density value. **E**) Schematic
1352 representation of how the interactions and the embedment into the membrane of PRLR contribute to
1353 the co-structure formation. The data from the simulations correspond to those of the production stage
1354 (see methods).
1355
1356 **Figure supplement 1**: *Protein – lipid interactions of PRLR-ICD_{LID1} obtained from CG-MD*
1357 *simulations using the martini 3.0b3.2 forcefield*
1358 **Figure supplement 2**: Complementary analysis of the Protein e Protein – lipid interactions of PRLR-
1359 ICD_{LID1} obtained from CG-MD simulations.
1360

1361 **Fig. 4. Protein – lipid interactions of the JAK2-FERM-SH2 PRLR-ICD$_{LID1}$ complex obtained**
1362 **from CG-MD simulations**. **A)** Schematic representation of the simulated system. Combined **B)**
1363 JAK2-FERM-SH2-lipid and **C)** PRLR-ICD$_{LID1}$-lipid contact frequency histograms for the 16 CG
1364 simulations of the JAK2-FERM-SH2 +PRLR-ICD$_{LID1}$+ POPC:POPS:PI(4,5)P_2 system. **D)**
1365 Distribution of the orientations adopted by the JAK2-FERM-SH2 + PRLR-ICD$_{LID1}$ complex when
1366 bound to lipids taken from the 16 simulations with POPC:POPS:PI(4,5)P_2 in the lower-leaflet. The
1367 snapshots surrounding the map correspond to representative conformations of the highlighted states
1368 also indicating the fraction total bound time for which each state was observed. Representative
1369 conformations of **E)** State 2 and **F)** State 4. The grey cylinder depicts the position where PRLR-TMD
1370 should be located. Representative protein-lipid contact histograms for **G)** State2 and **H)** State4
1371 colored as in panels B and C.
1372 **Figure supplement 1**: *Analysis of the JAK2-FERM-SH2- PRLR-ICD$_{LID1}$ AA-MD simulation***.**
1373 **Figure supplement 2.** *Complementary analysis of Protein – lipid interactions of the JAK2-FERM-*
1374 *SH2 PRLR-ICD$_{LID1}$ complex obtained from CG-MD simulations*
1375 **Figure supplement 3.** *Snapshots of the different binding states observed for the JAK2-FERM-SH2 –*
1376 *PRLR-ICD$_{LID1}$ complex with the complete structural model of JAK2*
1377
1378 **Fig. 5. PRLR variants with mutations in lipid interacting residues exhibit decreased PRL-**
1379 **stimulated STAT5 activation in AP1-2PH-PLCδ-GFP cells. A)** NMR intensity changes of
1380 ICD$_{K235-G313}$ WT, K4G, K4E, φ4G and GAG variants upon titration with 5x, 10x and 25x molar
1381 excess C_8-PI(4,5)P_2 plotted against residue number. **B)** The PRLR variants (WT, K4G, K4E, φ4G,
1382 3GAG) were transiently transfected in AP1 cells stably expressing the 2PH-PLCδ-GFP construct
1383 which visualizes the plasma membrane by binding PI(4,5)P_2. The cells were subsequently analysed
1384 by immunofluorescence microscopy, using antibodies against PRLR (magenta) and GFP (green), as
1385 well as DAPI (blue) to mark nuclei. To the right, examples of an average line-scan for each PRLR
1386 variant is shown. The fluorescence intensity depicted along the white line drawn (arrow) and green
1387 fluorescence (plasma membrane) was used to divide the line in a plasma membrane section and
1388 intracellular section, and relative membrane localization was calculated as the average fluorescence
1389 of PRLR in the membrane section divided by that in the intracellular section. **C, D)** AP1-2PH-PLCδ-
1390 GFP cells were transiently transfected with PRLR variants (WT, K4G, K4E, φ4G, 3GAG, K2E$_{253}$,
1391 K2E$_{261}$) and incubated overnight followed by serum starvation for 16-17 h and were subsequently
1392 incubated with or without 10 nM prolactin for 30 min. The resulting lysates were analysed by western
1393 blot for STAT5, pSTAT5 (Y964), PRLR, β-actin and p150 levels. The immunoblots are
1394 representative of three biological replicates. **E**) Ratio of plasma membrane localized receptor
1395 compared to intracellular receptor, analysed by line-scans as in B. Each point represents an individual
1396 cell, and data are based on three independent biological experiments per condition. Graphs show
1397 means with SEM error bars. *P<0.05, **P<0.01 and ****P<0.0001. One-way ANOVA compared to
1398 WT, unpaired**. F)** Quantification of western blot results shown as pSTAT5 normalized to total
1399 STAT5, relative to the WT condition. Graphs show means with SEM error bars. *P<0.05 and
1400 **P<0.01. One-way ANOVA compared to WT, unpaired.
1401 **Source file 1**: Raw western blots (relating to *figure 5C*)
1402 **Source file 2**: Raw western blot (relating to *figure 5D*)

1403 **Source file 3**: Data summaries (relating to *figure 5E,F*)
1404 **Figure supplement 1**: *Chemical shift perturbations of* $ICD_{K235\text{-}G313}$ *of A) WT, B) K4E, C) GAG, D)*
1405 *K4G and E) ϕ4G variants.*
1406 **Figure supplement 2:** ^{15}N R_2 *relaxation rates of* $ICD_{K235\text{-}G313}$ *of WT (grey bars), K4G (blue dots)*
1407 *and ϕ4G (red squares) variants.*
1408
1409 **Fig. 6. Model of how co-structure formation between JAK2, PRLR and PI4(4,5)P_2 may**
1410 **contribute to signalling fidelity.** The suggested states in signalling would be **A**) the inactive state of
1411 the co-structure exemplified by the Flat orientation. **B**) The hormone bound state expemplfied by the
1412 co-structure in the Y orientation. **C**) Phosphorylation of PIP(4,5)P_2 to PI(3,4,5)P_3 for which the PRLR
1413 has no affinity may lead to downregulation and/or termination of signalling. The colour scheme of
1414 the proteins is identical to Fig.4.
1415

1416 **Figure supplements and Supplementary files**

1417

1418 The prolactin receptor scaffolds Janus kinase 2 via co-structure 1419 formation with phosphoinositide-4,5-bisphosphate

1420 Raul Araya-Secchi[1,2], Katrine Bugge[3#], Pernille Seiffert[3#], Amalie Petry[4], Gitte W. Haxholm[3],
1421 Kresten Lindorff-Larsen[3], Stine F. Pedersen[4*], Lise Arleth[1*] and Birthe B. Kragelund[3*]
1422
1423 [1]Structural Biophysics, Section for Neutron and X-ray Science, Niels Bohr Institute, University of
1424 Copenhagen, 2100 Copenhagen, Denmark.
1425 [2] Facultad de Ingenieria Arquitectura y Diseño, Universidad San Sebastian, Bellavista 7, Santiago,
1426 Chile.
1427 [3]Structural Biology and NMR Laboratory (SBiNLab), Department of Biology, University of
1428 Copenhagen, 2200 Copenhagen, Denmark.
1429 [4]Section for Cell Biology and Physiology, Department of Biology, University of Copenhagen, 2200
1430 Copenhagen N, Denmark
1431
1432

1433 **Overview of contents:**

1434 **Figure supplements for main figures:**

1435 **Figure 2 – Figure supplement** 1: ^{15}N, ^{1}H-HSQCs of $TMD_{F206-V240}$, TMD-$ICD_{F206-S270}$ in DHPC micelles (A)
1436 and TMD-$ICD_{F206-S270}$ in POPC SUVs (B)

1437 **Figure 2 – Figure supplement** 2: Cα secondary chemical shifts of $ICD_{G236-Q396}$

1438 **Figure 3 - Figure supplement 1:** Protein – lipid interactions of PRLR-ICD_{LID1} obtained from CG-MD
1439 simulations using the martini 3.0b3.2 forcefiel

1440 **Figure 3 - Figure supplement 2:** Complementary analysis of the Protein – lipid interactions of PRLR-ICD_{LID1}
1441 obtained from CG-MD simulations.

1442 **Figure 4 – Figure supplement** 1: Analysis of the JAK2-FERM-SH2- PRLR-ICD_{LID1} AA-MD simulation.

1443 **Figure 4 – Figure supplement** 2: Complementary analysis of Protein – lipid interactions of the JAK2-FERM-
1444 SH2 PRLR-ICDLID1 complex obtained from CG-MD simulations

1445 **Figure 4 – Figure supplement** 3: Snapshots of the different binding states observed for the JAK2-FERM-
1446 SH2 – PRLR-ICDLID1 complex with the complete structural model of JAK2

1447 **Figure 5 – Figure supplement** 1: Chemical shift pertubations of $ICD_{K235-G313}$ of A) WT B) K4E, C) GAG, D)
1448 K4G and E) ϕ4G variants.

Figure 5 – Figure supplement 2: ^{15}N R_2 relaxation rates of $ICD_{K235-G313}$ of WT (grey bars), K4G (blue dots) and ϕ4G (red squares) variants.

Supplementary files not directly related to any main figures:

Movie 1: Y State (STATE 2) from the JAK2-FERM-SH2 PRLR-$ICD_{K235-E284}$ complex simulated near a bilayer containing PI(4,5)P_2 : Representative trajectory showing State 2 (Y). Protein and lipids colored as in Fig. 4

Movie 2: FLAT State (STATE 4) from the JAK2-FERM-SH2 PRLR-$ICD_{K235-E284}$ complex simulated near a bilayer containing PI(4,5)P_2 : Representative trajectory showing State 4 (Y). Protein and lipids colored as in Fig. 4

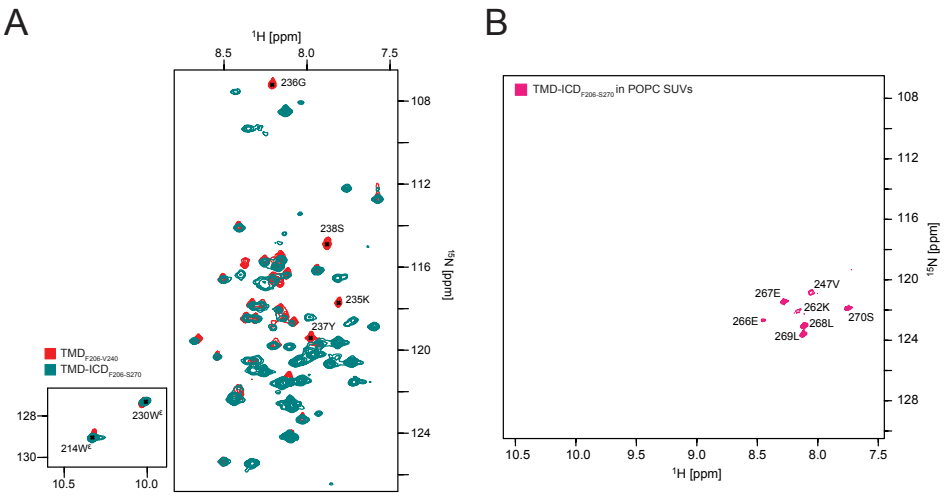

Figure 2 – figure supplement 1. ^{15}N, ^{1}H-HSQC spectra of A) $TMD_{F206-V240}$ and $TMD\text{-}ICD_{F206-S270}$ in DHPC micelles, and (B) $TMD\text{-}ICD_{F206-S270}$ in POPC SUVs.

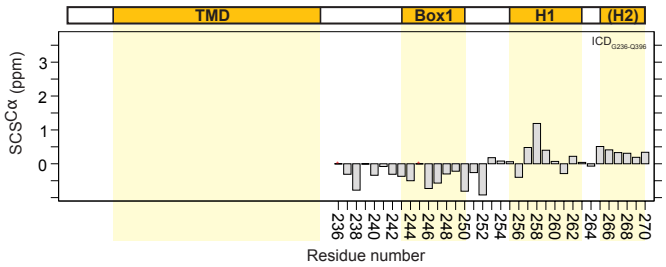

Figure 2 – figure supplement 2. Cα secondary chemical shifts of $ICD_{G236-Q396}$.

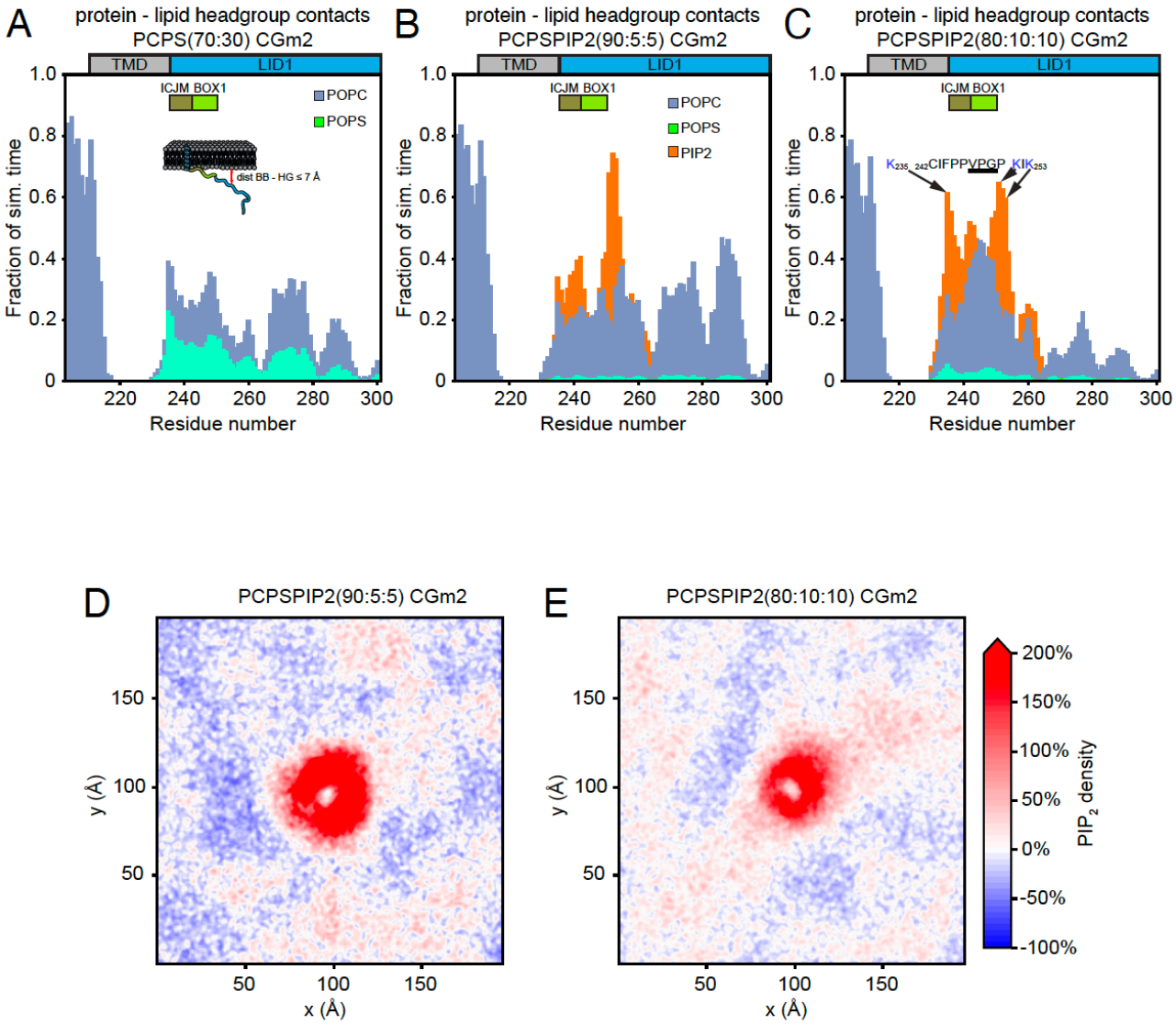

Figure 3 – figure supplement 1. Protein – lipid interactions of PRLR-ICD$_{LID1}$ obtained from CG-MD simulations using the martini 2.2 forcefield. *(A-C)* Protein – lipid-headgroups contact histograms from: (A) the PRLR-ICD$_{LID1}$ POPC:POPS (70:30) CGm2 simulation, (B) PRLR-ICD$_{LID1}$ POPC:POPS:PI(4,5)P$_2$ (90:5:5) CGm2 simulation and (C) PRLR-ICD$_{LID1}$ PRLR-ICD$_{LID1}$POPC:POPS:PI(4,5)P$_2$ (80:10:10) CGm2 simulation.

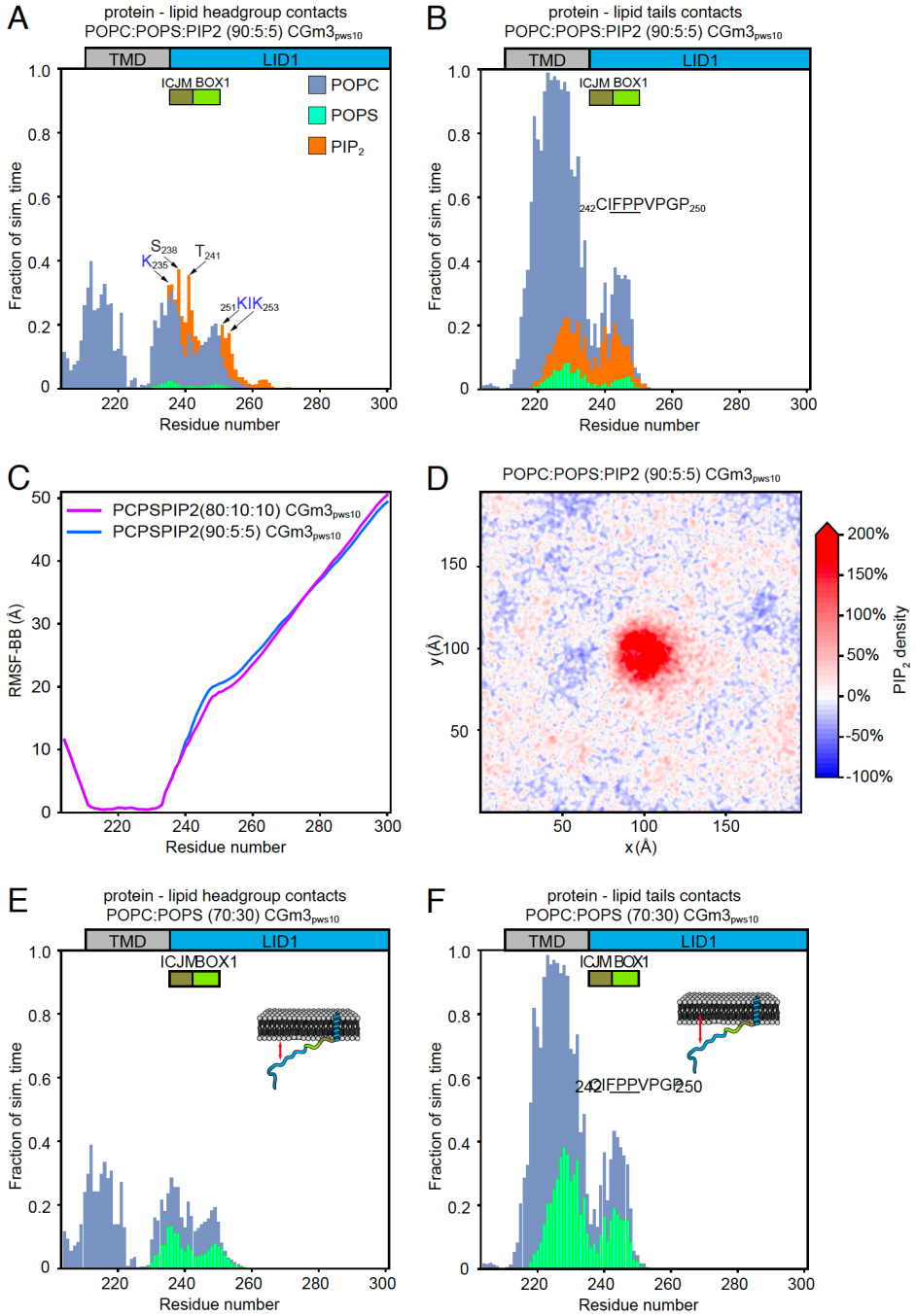

Figure 3 – figure supplement 2: Complementary analysis of protein – lipid interactions of PRLR-ICD$_{LID1}$ obtained from CG-MD simulations using the martini 3.0b3.2 forcefield. (A-B) Protein – lipids contact histograms from the PRLR-ICD$_{LID1}$ POPC:POPS:PI(4,5)P$_2$ (90:5:5) CGm3$_{pws10}$ simulation. (A) Contacts between the protein and lipid headgroups. (B) Contacts between the protein and the acyl chains of the lipids. (C) RMSF of the BB beads obtained from the PRLR-ICD$_{LID1}$POPC:POPS:PI(4,5)P$_2$ (80:10:10) CGm3$_{pws10}$ simulation (Magenta line) and the PRLR-ICD$_{LID1}$ POPC:POPS:PI(4,5)P$_2$ (90:5:5) CGm3$_{pws10}$ simulation (blue line). (D) Average PI(4,5)P$_2$ density map (*xy*-plane) taken from the PRLR-ICD$_{LID1}$ + POPC:POPS:PI(4,5)P$_2$(90:5:5) CGm3$_{pws10}$ simulation. (E-F) Protein – lipids contact histograms from the PRLR-ICD$_{LID1}$ POPC:POPS (30:70) CGm3$_{pws10}$ simulation. (E) Contacts between the protein and lipid headgroups. (F) Contacts between the protein and the acyl chains of the lipids. In A-B and E-F protein – lipid contacts are defined as in Figure 3.

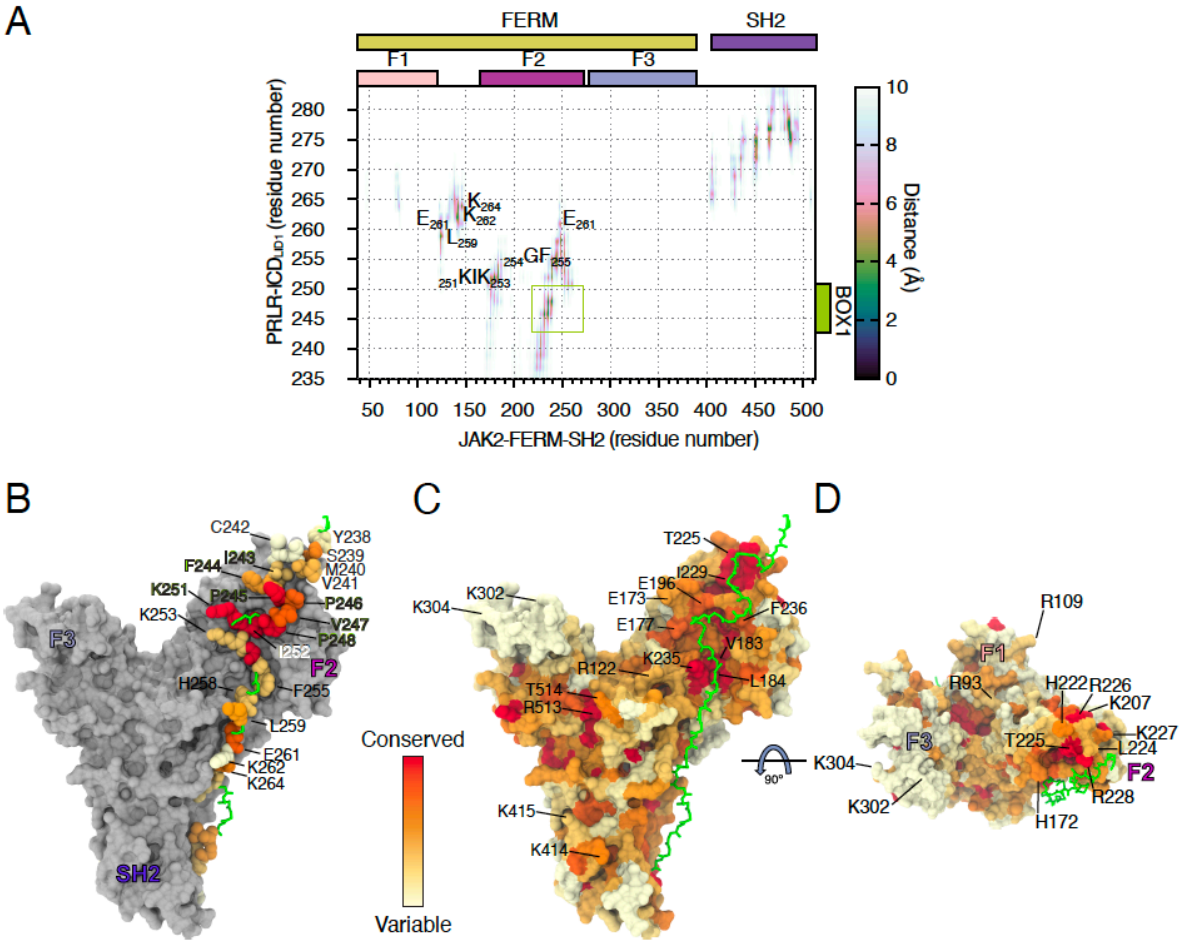

Figure 4 - Figure supplement 1: **Analysis of the JAK2-FERM-SH2- PRLR-ICD$_{K235-H300}$ AA-MD simulation.** A) Average distance map between JAK2-FERM-SH2 and PRLR-ICD$_{K235-H300}$ obtained from the all-atom MD simulation. (B) Conservation of residues from PRLR in contact with JAK2-FERM-SH2 (see A). Residues with green label correspond to BOX1. (C-D) Conservation JAK2-FERM-SH2 oriented as state 2 (see Fig. 4E). Labeled residues correspond to residues that contact PRLR (see A) or that contact the lipids on states 2 and 4 (see Fig. 4E-H).

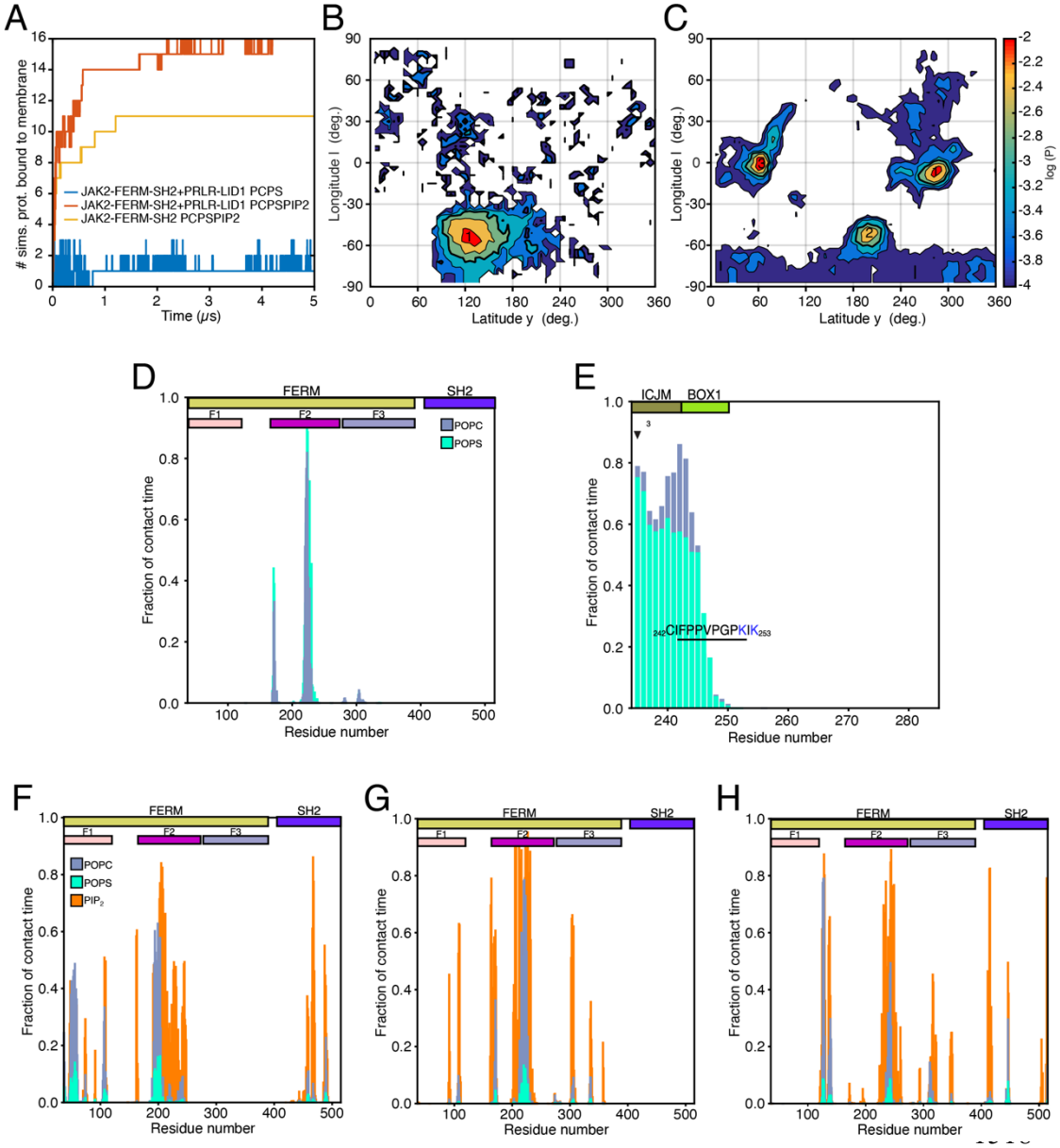

Figure 4 - Figure Supplement 2. Complementary analysis of Protein – lipid interactions of the JAK2-FERM-SH2 PRLR-ICD$_{K235-H300}$ complex obtained from CG-MD simulations (A) Number of simulations where protein is bound to the lower-leaf of the bilayer for the simulations containing: the JAK2-FERM-SH2 + PRLR-ICD$_{K235-H300}$ complex near a POPC:POPS(70:30) bilayer (blue line) and the JAK2-FERM-SH2 + PRLR-ICD$_{K235-H300}$ complex (red line) and the apo JAK2-FERM-SH2 (orange line)near a POPC:POPS:PI(4,5)P_2 (80:10:10) bilayer. (B-C) Distribution of the orientations adopted by (B) the JAK2-FERM-SH2 + PRLR-ICD$_{K235-H300}$ complex when bound to lipids taken from the simulations with POPC:POPS(70:30) in the lower-leaflet and (C) the apo JAK2-FERM-SH2 when bound to lipids taken from the simulations with POPC:POPS:PI(4,5)P_2 (80:10:10) in the lower-leaflet. (D-E) Representative protein-lipid contact histograms for State 1 observed for the JAK2-FERM-SH2 + PRLR- ICD$_{K235-H300}$ complex near a POPC:POPS(70:30) bilayer. (F-H) Representative protein-lipid contact histograms for States 1, 2 and 3 observed for the apo JAK2-FERM-SH2 near a POPC:POPS:PI(4,5)P_2 (80:10:10) bilayer.

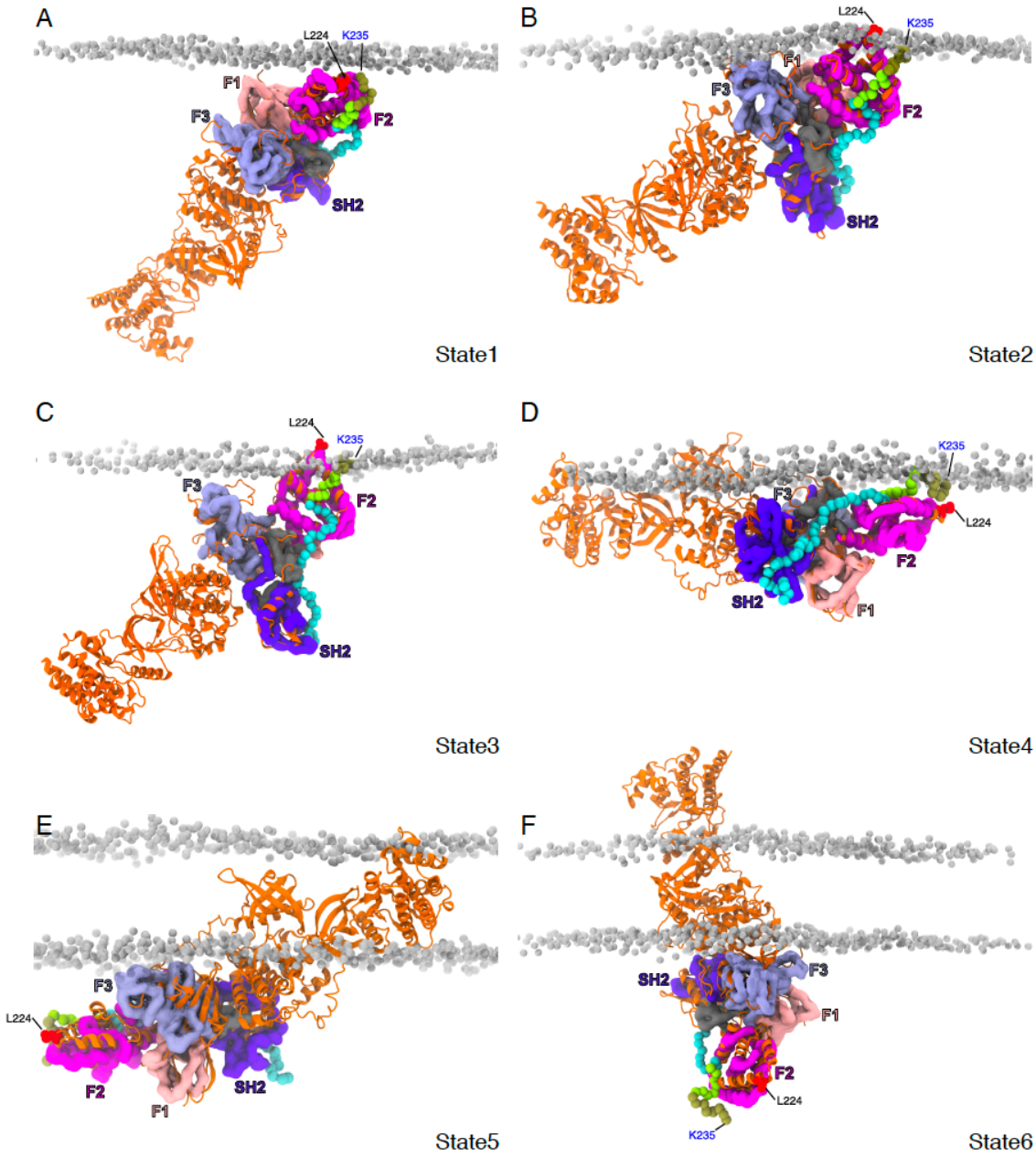

Figure 4 - Figure Supplement 3. Snapshots of the different binding states observed for the JAK2-FERM-SH2 – PRLR-ICD$_{K235\text{-}H300}$ complex with the complete structural model of JAK2 (obtained from AF2-EBI database). In each panel the CG JAK2-FERM-SH2 – PRLR-ICD$_{K235\text{-}H300}$ complex is depicted and colored as in Fig. 4. The full-length JAK2 model is shown in cartoon representation colored orange. near a POPC:POPS(70:30) bilayer. (F-H) Representative protein-lipid contact histograms for States 1, 2 and 3 observed for the apo JAK2-FERM-SH2 near a POPC:POPS:PI(4,5)P_2 (80:10:10) bilayer.

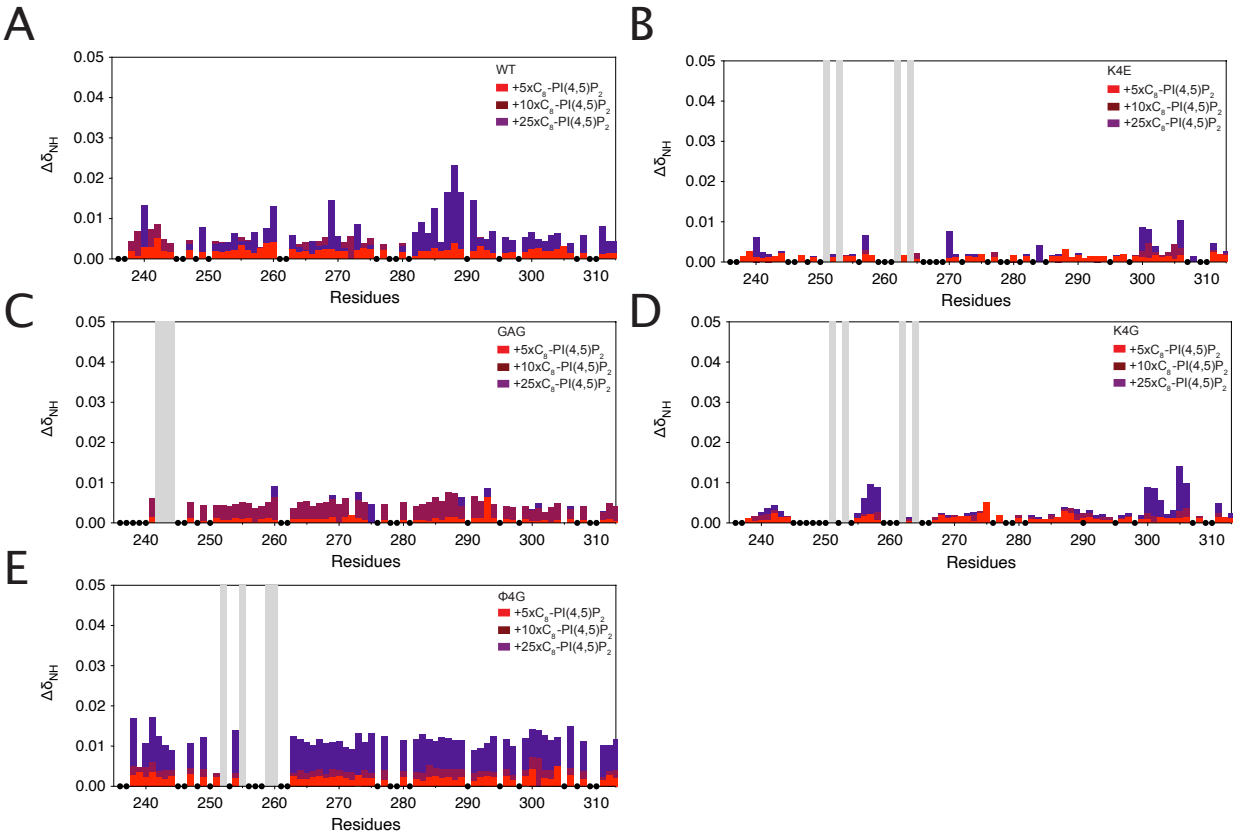

1543

1544 **Figure 5 – Figure supplement** 1: Chemical shift perturbations of $ICD_{K235-G313}$ of A) WT B) K4E, C) GAG, D)
1545 K4G and E) ϕ4G variants.

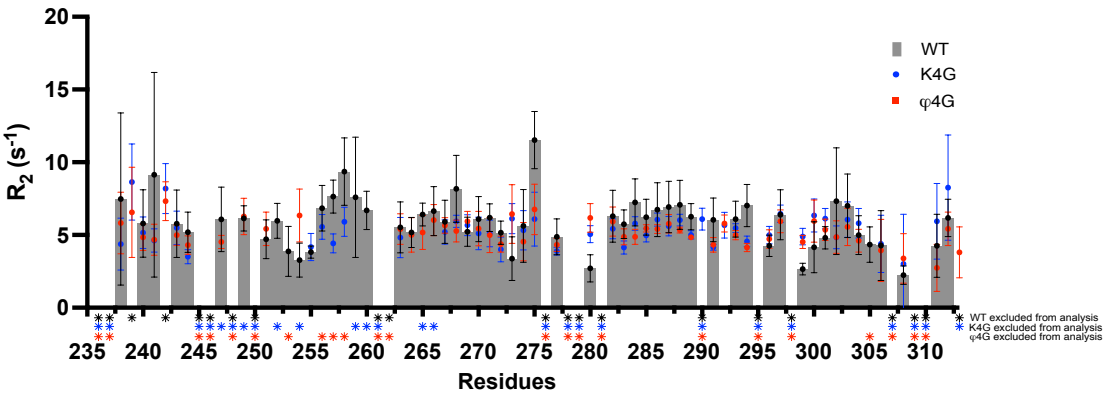

1546

1547 **Figure 5 – Figure supplement** 2: ^{15}N R_2 relaxation rates of $ICD_{K235-G313}$ of WT (grey bars), K4G (blue dots)
1548 and ϕ4G (red squares) variants. Stars indicate signals excluded from the analysis either because it is a
1549 proline, signals are overlapping or a poor exponential fit.